Simulation and characterization of the laminar separation bubble over a NACA-0012 airfoil as a function of angle of attack

Eltayeb Eljack [©],[1,*] Julio Soria [©],[2] Yasir Elawad [©],[3] and Tomohisa Ohtake[4]

[1]*Mechanical Engineering Department, University of Khartoum, Khartoum 11115, Sudan*

[2]*Laboratory for Turbulence Research in Aerospace and Combustion, Department of Mechanical and Aerospace Engineering, Monash University, Melbourne, Clayton Victoria 3800, Australia*

[3]*Aeronautical Engineering Department, King Abdulaziz University, Jeddah, Jeddah 21589, Saudi Arabia*

[4]*Department of Aerospace Engineering, Nihon University, Tokyo 101-8308, Japan*

This study examines the effects of angle of attack on the characteristics of the laminar separation bubble (LSB), its associated low-frequency flow oscillation (LFO), and the flow field about a NACA-0012 airfoil at Reynolds number of 5×10^4 and 9×10^4, Mach number of 0.4, and several angles of attack near stall. In the range of the investigated angles of attack, statistics of the flow field suggest the existence of three distinct angle-of-attack regimes. At angles of attack lower than the stall angle of attack, the mean flow field is attached, a short bubble is formed, and the flow field is not much affected by the LFO. At angles of attack higher than the stall angle of attack and lower than the angle of attack of maximum LFO, the flow field undergoes a transition process in which the LFO develops until the flow field reaches a quasiperiodic switching between separated and attached flow and the LSB switches between short and long bubble. At angles of attack higher than the angle of attack of maximum LFO, the mean flow field is massively separated, an open bubble is formed, and the LFO gradually loses momentum and becomes unable to reattach the flow until the airfoil approaches the angle of a full stall. These angle-of-attack regimes have, to the best of the authors' knowledge, not been reported in the literature before.

I. INTRODUCTION

Applications that operate at low Reynolds numbers, $\text{Re}_c < 10^6$ based on the free-stream velocity and airfoil chord, have steadily increased over the past four decades. These applications include unmanned aerial vehicles, micro aerial vehicles, low-pressure turbines, low-pressure compressors, helicopter blades, and vertical axis wind turbines. Airfoils operating at low Reynolds number have proclivity to induce a laminar separation bubble (LSB) on their upper surface. The LSB affects the boundary layer on the airfoil surface and consequently the stalling characteristics of airfoils Tani [1] and Mueller *et al.* [2].

Owen and Klanfer [3] classified the LSB into two distinct formats of short and long bubble. The bubble is short if the ratio of the bubble length to the displacement thickness at the point of separation is in the order of 100, whereas the bubble is termed long if the ratio is in the order of 400. A short bubble has little effect on the external potential flow, while the long bubble has a more notable influence. At certain conditions, a short bubble suddenly alters to a long bubble or a fully separated flow without any subsequent reattachment, which is termed bubble bursting. The first observations and descriptions of the LSB were reported by Melvill Jones [4]. After that, the

---

*Corresponding author: emeljack@uofk.edu

structure of the LSB was investigated in the work of Young and Horton [5], and its averaged shape was described by Horton [6]. A landmark work on LSBs was carried out by Gaster [7]. He wanted to eliminate the effect of the airfoil geometry and generate data of different LSBs. The author invented a brilliant model that allowed him to vary both the Reynolds number and the pressure distribution. The model was a flat plate with an adjustable pressure distribution. He used the model to carry out a series of experiments that provided enough data sets for him to characterize the LSB and its bursting process. He found that the structure of the LSB depends on two parameters. The first parameter is the Reynolds number of the separated boundary layer, and the second parameter is a function of the pressure rise over the region occupied by the bubble. Then he determined conditions for the bursting of short bubbles by a unique relationship between these two parameters. The structure, stability, and bursting of the LSB were investigated extensively in these studies. However, the primary causes that triggers the instability of the LSB were not determined. A copious amount of research was carried out at prestall conditions to investigate the stability of the LSB [8–19].

The bubble breathing, vortex shedding, and/or flapping of the shear layer triggers low-frequency flow oscillation (LFO) at prestall conditions as a consequence of changing the boundary conditions or perturbing the free stream. However, at near-stall conditions, the LSB becomes unstable and switches the flow between attached and separated phases. Consequently, the flow field and the aerodynamic forces oscillate at a low frequency in a quasiperiodic self-sustained process. Such an unusually low-frequency oscillation in the flow field was investigated and observed in numerical and experimental studies [20–30].

The presence of the bubble significantly deteriorates the aerodynamic performance, such as loss of lift, undesirable change in the moment, and increase in the drag. Flow oscillations due to bubble shedding and sudden airfoil stalling due to bubble bursting are direct consequences of the complex and random behavior of the LSB. Mccullough and Gault [31] classified the airfoil stall into three main categories: (1) leading-edge, (2) thin-airfoil, and (3) trailing-edge stall. The leading-edge stall results from the flow separation near the leading-edge without any subsequent reattachment downstream of the separation. In the thin-airfoil stall, the flow reattaches downstream the separation bubble, and then the reattachment point moves toward the trailing-edge as the angle of attack increases. The trailing-edge stall initiates at the trailing edge where the flow separates, and the separation point moves toward the leading edge as the angle of attack increases.

Preliminary results of the data sets used in the present work were documented in Eljack [28], Elawad and Eljack [29], and a detailed underlying mechanism that generates, sustains, and controls the LFO was presented by Eljack and Soria [30]. The objective of the present study is to examine the effects of the angle of attack on the characteristics of the LSB, its associated LFO, and the flow field around a NACA-0012 airfoil at near-stall conditions. A conditional time and phase averaging are used to characterize the flow field. The characteristics of the flow field, the LSB, and the LFO are provided along with careful comparisons with existing experimental and numerical work. Similarities are discussed in detail, and discrepancies are justified wherever necessary.

II. MATHEMATICAL MODELING

In the present study, the fluid flow is governed by the viscous-compressible Navier-Stokes equations. The nondimensional analysis of these equations is achieved using the following nondimensional variables:

$$u_j = \frac{u_j^*}{u_r^*}, \quad \rho = \frac{\rho^*}{\rho_r^*}, \quad T = \frac{T^*}{T_r^*}, \quad x_j = \frac{x_j^*}{c}, \quad \mu = \frac{\mu^*}{\mu_r^*}, \quad P = \frac{P^*}{\rho_r^* u_r^{*2}}, \quad t = \frac{t^* u_r^*}{c},$$

where

$$u_j = [u_1, \ u_2, \ u_3]^\mathsf{T} \quad \text{and} \quad x_j = [x, \ y, \ z]^\mathsf{T}.$$

Here ρ, T, and μ are the fluid density, temperature, and dynamic viscosity, respectively. p is the flow pressure, t is time, and c represents the airfoil chord length. The subscript r denotes the reference

variables, and the symbol $*$ indicates the dimensional variables. The nondimensional form of the three-dimensional compressible Navier–Stokes equations can be written in vector form as

$$\frac{\partial Q}{\partial t} + \frac{\partial F_j}{\partial x_j} = \frac{\partial G_j}{\partial x_j},$$ (1)

where

$$Q = \begin{bmatrix} \rho \\ \rho u_1 \\ \rho u_2 \\ \rho u_3 \\ \rho(D+E) \end{bmatrix}, \quad F_j = u_j Q + \begin{bmatrix} 0 \\ \delta_{1j}p \\ \delta_{2j}p \\ \delta_{3j}p \\ pu_j \end{bmatrix}, \quad G_j = \begin{bmatrix} 0 \\ \sigma_{1j} \\ \sigma_{2j} \\ \sigma_{3j} \\ \sigma_{kj}u_k - b_j \end{bmatrix},$$

where $D = \frac{T}{\gamma(\gamma-1)M_\infty^2}$ and $E = \frac{1}{2}u_j.u_j^T$.

Q is a vector including the conservative flow variables, F is the inviscid flux vector, and G is the viscous flux vector. σ_{ij} is the viscous stress tensor, and the term b_j is given by

$$b_j = J\frac{\partial T}{\partial x_j} \quad \text{and} \quad J = \frac{\mu(T)}{(\gamma-1)Pr\ Re_c\ M_\infty^2},$$

where $M_\infty = 0.4$ is the reference Mach number, $\gamma = 1.4$ is the specific heat ratio, $Re_c = 5 \times 10^4$ and 9×10^4 are the chord Reynolds number, and $Pr = 0.72$ is the Prandtl number. The dynamic viscosity μ is calculated using the dimensionless form of Sutherland's law:

$$\mu(T) = T^{\frac{3}{2}}\frac{1+C}{T+C}, \quad C = 0.3686.$$

The relation between T, ρ and p is given by the ideal gas law:

$$T = \gamma M_\infty^2 \frac{p}{\rho}.$$

The viscous stress tensor σ_{ij} is given by

$$\sigma_{ij} = \frac{\mu(T)}{Re}\left(\frac{\partial u_i}{\partial x_j} + \frac{\partial u_j}{\partial x_i} - \frac{2}{3}\delta_{ij}\frac{\partial u_k}{\partial x_k}\right),$$

where δ_{ij} is the Kronecker delta.

For LES, any flow variable ψ is decomposed for large and small scales, therefore $\psi = \ddot{\psi} + \dot{\psi}$. $\ddot{\psi}$ and $\dot{\psi}$ represent the large and small scales, respectively. For compressible flow, it is convenient to use $\tilde{\psi} = \overline{\rho\psi}/\overline{\rho}$ as a Favre-filtered flow variable (density weighted). By applying the Favre filtering to Eq. (1), the resultant filtered form is given by

$$\frac{\partial \hat{Q}}{\partial t} + \frac{\partial \hat{F}_j}{\partial x_j} = \frac{\partial \hat{G}_j}{\partial x_j},$$ (2)

where $\hat{Q}$, $\hat{F}_j$, and $\hat{G}_j$ are the Favre-filtered counterparts of Q, F_j, and G_j, respectively. The SGS stress tensor τ_{ij} expresses the effect of small scales on the residual stress, and it is modeled as

$$\tau_{ij} = \overline{\rho}(\widetilde{u_i u_j} - \tilde{u}_i\ \tilde{u}_j).$$ (3)

The models used in the present study are based on the idea of an eddy viscosity ν_t. Consequently, the stress tensor is given by

$$\tau_{ij} - \frac{1}{3}\delta_{ij}\tau_{kk} = 2\nu_t\tilde{S}_{ij},$$

where τ_{kk} is the isotropic part of the τ_{ij} and the strain rate tensor is defined by

$$\tilde{S}_{ij} = \frac{1}{2}\left(\frac{\partial \tilde{u}_i}{\partial x_j} + \frac{\partial \tilde{u}_j}{\partial x_i}\right).$$

By applying the dimensional analysis to ν_t, it gives

$$\nu_t \propto I_{SGS} \, u_{SGS}, \tag{4}$$

where I_{SGS} and u_{SGS} are the length and velocity scales for the unresolved motion, respectively. Several models are developed to describe the effect of the SGS stress components. The mixed timescale (MTS) model was developed by Inagaki *et al.* [32]. This model is constructed without using any explicit wall damping function to overcome the drawbacks of other SGS models. In the MTS model, the expression of ν_t which is given in Eq. (4) is modified to be given by

$$\nu_t \propto T_{SGS} \, u_{SGS}^2,$$

where T_{SGS} is a timescale, and u_{SGS} is a velocity scale, which can be calculated using

$$u_{SGS}^2 = (\bar{u} - \hat{\bar{u}})^2,$$

where a top hat filtering $\hat{()}$ denotes a second filtering process. By applying this formula, the ν_t approaches zero in the laminar flow region because the u_{SGS} also approaches zero and the flow is fully resolved. This can be considered as an important benefit of using the MTS model since it does not need any additional damping functions. The term T_{SGS} is given by

$$T_{SGS}^{-1} = \left(\frac{\bar{\Delta}}{u_{SGS}} \right)^{-1} + \left(\frac{C_i}{|\bar{S}|} \right)^{-1},$$

where $\bar{\Delta}$ represents the filter size and C_i is a fixed parameter (in the current study $C_i = 10$). Inagaki *et al.* [32] suggested the timescale as $1/|\bar{S}|$. They found that $\nu_t \propto u_{SGS}^2/|\bar{S}|$ exhibits good agreement with other SGS models that have a wall damping function. However, it was not appropriate to implement this eddy viscosity in a region away from the wall where the problem of dividing by zero can arise. This problem was solved by adding another timescale $\bar{\Delta}/u_{SGS}$, which was proposed by Yoshizawa *et al.* [33]. Therefore, the ν_t can be expressed as

$$\nu_t = C_{MTS} \, T_{SGS} \, u_{SGS}^2,$$

where C_{MTS} is a fixed model parameter (in the current study $C_{MTS} = 0.03$).

There are two methods to overcome grid to grid oscillations. The first method is by adding an artificial dissipation to Navier-Stokes equations. The second method is by applying a filter to the flow field for the small scales without disturbing the large scales. In the current study, the latter method is used. Visbal and Rizzetta [34] found that to maintain numerical stability, it is convenient to use compact schemes of order equal or greater than the order of spatial discretization. The spatial filtering is applied using explicit low-pass filter to the unfiltered field to obtain an approximate solution:

$$\alpha_f \, \bar{\hat{Q}}_{i-1} + \bar{\hat{Q}}_i + \alpha_f \, \bar{\hat{Q}}_{i+1} = \sum_{n=0}^{2} \frac{a_n}{2} (\hat{Q}_{i+n} + \hat{Q}_{i-n}).$$

$\bar{\hat{Q}}_i$ and $\hat{Q}_i$ are the filtered and unfiltered values at point i, respectively. α_f is a free parameter in the range of $0 \leqslant \alpha_f \leqslant 0.5$. The coefficients a_n are derived by matching the corresponding Taylor series coefficients based on the order of accuracy. The low-pass and high-pass filters remove the small and large scales, respectively. A fourth-order tridiagonal filter is applied in the current study [35]. It is unnecessary to implement the whole filtered function but just a part of it according to the following equation:

$$\bar{\bar{Q}} = \hat{Q} - \sigma(\hat{Q} - \bar{Q}),$$

where $\bar{\bar{Q}}$ is the resulting filtered vector and σ is the filter constant between 0 and 1. If $\sigma = 0$, then no filtering is applied. In the present study $\sigma = 0.25$.
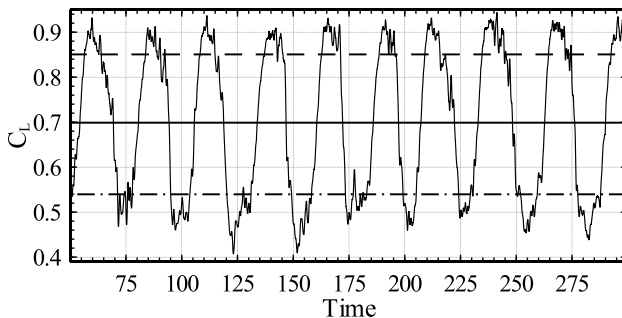
FIG. 1. Time history of the lift coefficient at $Re_c = 9 \times 10^4$ and the angle of attack of $11.0°$. The dashed, solid, and dash-dot horizontal lines show the high-lift, mean-lift, and low-lift time average, respectively.

III. CONDITIONAL TIME AND PHASE AVERAGING

The signal of the lift coefficient at each angle of attack was used as a reference to conditionally time averaging the flow field. The time average of an instantaneous variable of the flow field, $< \psi >$, was defined on three different levels a mean-lift, a high-lift, and a low-lift time average. Figure 1 illustrates the concept of the conditional time averaging. The mean-lift average of the variable ($< \bar{\psi} >$) is simply the time average of all data samples of the variable. The high-lift average of the variable ($< \hat{\psi} >$) is the time average of all data samples that have values higher than the mean value. The low-lift average of the variable ($< \check{\psi} >$) is the average of all data samples that have values less than the mean value. The lift coefficient signal is used to identify the data samples that are above or below the mean. It is implemented by taking the mean of the lift coefficient at each angle of attack. The indices of data points of the time history of the lift coefficient that are above/below the mean of the lift coefficient are then stored in a high-lift/low-lift data files, respectively. The indices are then used to locate the data of other flow variables that are above/below their corresponding mean and consequently used to estimate the low-lift and high-lift time average for all of the flow variables. Thus, the conditional time averaging is synchronized for all variables so that at a given time step all variables are allocated to either the high-lift or low-lift regimes.

The previously defined conditional time average on three levels (high-lift, mean-lift, and low-lift) can be expanded to a series of 37 intervals that gives continues phase information of one complete cycle. Figure 2 illustrates the conditional phase-averaging process. The right-hand side of the figure shows time history of the lift coefficient at $Re_c = 9 \times 10^4$ and the angle of attack of $11.0°$. The
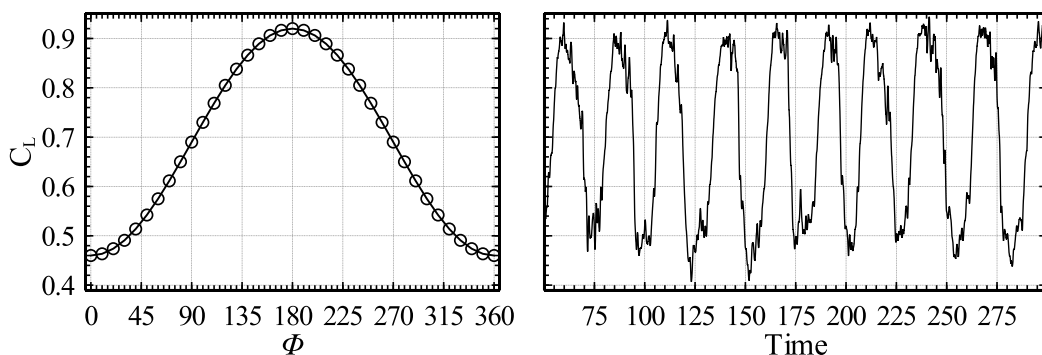

FIG. 2. The conditional phase-averaging process. Left: One sinusoidal cycle. Right: Time history of the lift coefficient at $Re_c = 9 \times 10^4$ and the angle of attack of $11.0°$.

TABLE I. Computational grid parameters.

Re_c	Grid	y^+	Δx^+	Δz^+	N_ξ	N_η	N_ζ	Total points
5×10^4	Grid 1	>1	<50	<50	637	320	86	17 530 240
	Grid 2	<1	<15	<15	780	320	101	25 209 600
	Grid 3	<1	<10	<10	980	320	151	47 353 600
9×10^4	Grid 1	<1	<20	<20	780	320	125	31 200 000
	Grid 2	<1	<15	<15	832	351	167	48 769 344
	Grid 3	<1	<10	<15	1192	351	167	69 871 464

left-hand side of the figure shows one sinusoidal cycle with a magnitude range of that of the lift coefficient divided into 36 equally distributed phases. The phase-averaging process is implemented in the same manner described and used for the conditional time averaging. The lift coefficient signal was split into an ascending part ($\Phi = 0°$ to $\Phi = 180°$) in which the lift is increasing with time and a descending part ($180° < \Phi < 360°$). The phase-averaging process was applied to the ascending and the descending lift coefficient and their corresponding data points. For a spanwise ensemble-averaged instantaneous flow variable $< \psi >$ the decomposition is

$$< \psi >=< \overline{\psi} > + \underbrace{< \psi'' > + < \psi' >}_{<\check{\psi}>}, \tag{5}$$

where $< \bar{\psi} >$ is the spanwise ensemble-averaged mean of the variable, $< \check{\psi} >$ is the spanwise ensemble-averaged total fluctuations of the variable, $< \psi'' >$ is the spanwise ensemble-averaged periodic fluctuations of the variable, and $< \psi' >$ is the spanwise ensemble-averaged turbulent fluctuations of the variable. The total fluctuations is the summation of the periodic fluctuations and the turbulent fluctuations.

IV. COMPUTATIONAL SETUP

In terms of the airfoil chord (c), the dimensions of the computational domain were set as follows: $L_\xi = 5c$ in the wake region, from the airfoil trailing edge to the outflow boundary in the streamwise direction, $L_\eta = 7.3c$ in the wall-normal direction (the C-grid radius), and $L_\zeta = 0.5c$ in the spanwise direction. Here ξ, η, and ζ are the curvilinear coordinates along the airfoil surface, in the wall-normal direction, and the spanwise direction, respectively. An adequate grid resolution is required to resolve the large eddies in the flow field. In the present study, three different C-grids for each Reynolds number are constructed with various distributions in ξ, η, and ζ direction. The LSB formation, elongation, and bursting processes should be well resolved, therefore; the grid resolution near the airfoil surface, especially on the suction side, is critical. In Table I, N_ξ, N_η, and N_ζ are the grid points in the ξ, η, and ζ direction, respectively. Figure 3 shows a close-up of the computational grid around the airfoil and a vector plot of the velocity field. As seen in the figure, the grid is very well refined in the LSB region.

The LES code utilized in the present simulations is an LES version of the direct numerical simulation (DNS) code written and validated by Jones *et al.* [36]. The Navier–Stokes equations were discretized using a fourth-order accurate explicit central difference scheme for the spatial discretization of the internal points. The fourth-order boundary scheme of Carpenter *et al.* [37] was used to treat points near and at the boundary. To preserve the spatial characteristics, the transformation metrics tensor $\hat{\xi}_{ij}$ were evaluated by using the same fourth-order scheme. The temporal discretization was performed using a low-storage fourth-order Runge-Kutta scheme. The integral characteristic boundary condition is applied at the free-stream and far-field boundaries [38]. The zonal characteristic boundary condition is applied at the downstream exit boundary [39], which is considered as a nonreflected boundary condition to overcome the circulation effects at the
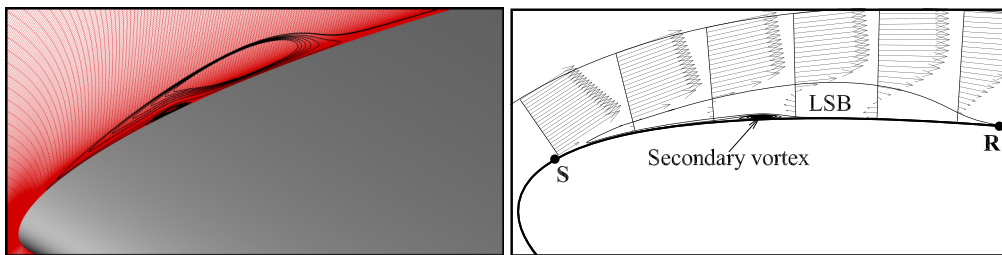
$\mathrm{Re}_c = 5 \times 10^4 \ and \ \alpha_s = 9.0°$ $\mathrm{Re}_c = 9 \times 10^4 \ and \ \alpha_s = 10.25°$

FIG. 3. Plots of the computational domain, grid distribution, and the LSB.

boundaries. The solution stability was improved by implementing an entropy splitting scheme [40]. The entropy splitting constant β was set equal to 2.0 [41]. The adiabatic and no-slip conditions are applied at the airfoil surface. The LSB, its associated LFO, and the flow field are inherently statistically two-dimensional. Therefore, a periodic boundary condition is applied in the spanwise direction for each step of the Runge-Kutta time steps. The internal branch-cut boundary was updated at each step of the Runge-Kutta scheme.

V. RESULTS AND DISCUSSION

LESs were carried out for the flow around the NACA-0012 airfoil at near-stall conditions. The simulations are carried out at Mach number of $M_\infty = 0.4$, Reynolds number of 5×10^4 and 9×10^4, and several angles of attack near stall. Reducing the Mach number of the numerical simulation to simulate the flow field at a near incompressible regime ($M_\infty < 0.1$) would considerably increase the computational cost. The entire domain was initialized using the free-stream conditions ($\rho_\infty = 1$, $\rho_\infty U_\infty = 1$, $\rho_\infty V_\infty = 0$, $\rho_\infty W_\infty = 0$, and $T_\infty = 1$). The simulations were performed with a time step of 10^{-4} nondimensional time units. Samples for statistics were collected once transition of the simulations has decayed and the flow became stationary in time after 50 nondimensional time units. Aerodynamic coefficients were sampled for each angle of attack at a frequency of 10 000 to generate two and a half million samples over a time period of 250 nondimensional time units. The locally time-averaged and spanwise ensemble-averaged pressure, velocity components, and Reynolds stresses were sampled every 50 time steps on the x-y plane. A data set of 20 000 x-y planes was recorded at a frequency of 204 at each angle of attack.

A. Three-dimensional instantaneous flow field

Figure 4 shows the instantaneous isosurfaces of the λ_2 criterion for the attached and separated phases of the flow field. The transition process from laminar to turbulent flow is captured in the simulations as seen in the figure. In the vicinity of the leading edge, the shear layer is separated and moved away from the airfoil surface. Two-dimensional laminar-like rolls develop along the separated shear layer. The Kelvin-Helmholtz instability extracts energy from the mean flow and feeds it into these rolls. The shear layer is a little bit distorted, a secondary spanwise instability develops to cause helical pairing between adjacent spanwise vortical structures, and eventually the two-dimensional rolls convert into three-dimensional Λ-shaped and hairpin structures. Consequently, the flow becomes turbulent. The left-hand side of Fig. 4 illustrates the attached phase of the flow field. As seen in the figure the separated shear layer is close to the airfoil surface, and the two-dimensional rolls form in the vicinity of the leading edge and subsequently break into three-dimensional structures. On the other hand, the separated shear layer moves away from the airfoil surface and toward the energetic free stream during the separated phase of the flow field as seen on the right side of the figure. Additionally, the location at which the two-dimensional
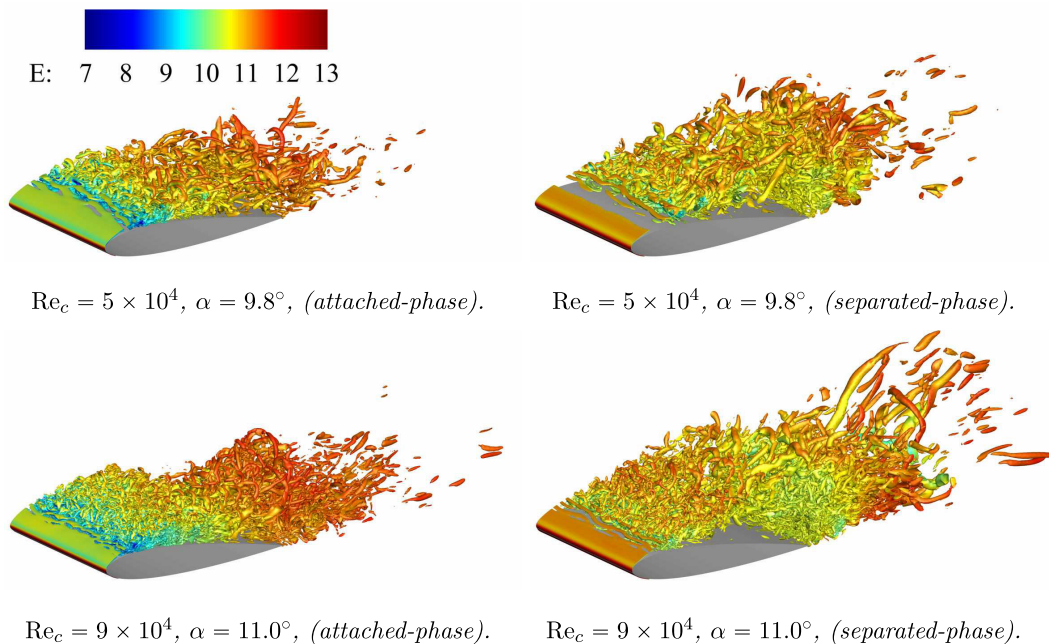
$\mathrm{Re}_c = 5 \times 10^4$, $\alpha = 9.8°$, (attached-phase).

$\mathrm{Re}_c = 5 \times 10^4$, $\alpha = 9.8°$, (separated-phase).

$\mathrm{Re}_c = 9 \times 10^4$, $\alpha = 11.0°$, (attached-phase).

$\mathrm{Re}_c = 9 \times 10^4$, $\alpha = 11.0°$, (separated-phase).

FIG. 4. Instantaneous λ_2-criterion isosurface ($\lambda_2 = -200$) colored by the total energy per unit mass (E).

rolls breakdown moves farther downstream during the separated phase. Thus, the two-dimensional structures break down close to the leading edge and consequently cause an early transition to turbulence during the attached phase, while the transition process takes place farther downstream during the separated phase of the flow field (late transition). In summary, Fig. 4 shows that the flow field switches between an attached phase and a separated phase. Consequently, a low-frequency global oscillation in the flow field is triggered. The velocity components, the pressure, and the aerodynamics coefficients oscillate accordingly at a low frequency.

B. Aerodynamic coefficients

The locally time-averaged pressure and skin-friction coefficients, C_p and C_f, are shown in Fig. 5. Ten profiles covering the range of angles of attack $9.25°$–$10.5°$ at $\mathrm{Re}_c = 5 \times 10^4$, and six profiles covering the range of angles of attack $10.25°$–$11.2°$ at $\mathrm{Re}_c = 9 \times 10^4$ are presented in the figure. The zoom-in window illustrates the distribution of C_p in the vicinity of the trailing edge in the range $0.6 \leqslant x/c \leqslant 1.0$. Near the airfoil leading edge, a laminar boundary layer develops, and the pressure coefficient decreases drastically. The boundary layer remains laminar until the pressure gradient changes from favorable to unfavorable. Consequently, the laminar boundary layer detaches at point **S** in Fig. 3 and travels away from the airfoil surface to create a region of separated flow near the surface. The flow then reattaches to the airfoil surface at point **R** in Fig. 3 and the LSB forms. The pressure coefficient exhibits a plateau across the bubble. As the angle of attack increases above the stall angle of attack the length of the bubble, in the mean sense, increases. Thus, the magnitude of the pressure coefficient across the bubble increases and the LSB covers a longer portion of the airfoil as seen in Fig. 5. Downstream the bubble the pressure gradient becomes adverse, but the flow is turbulent and has enough momentum to overcome new separation. At the trailing edge, the pressure coefficient shifts upwards gradually as the angle of attack increases as a consequence of the formation of a trailing-edge bubble (TEB).

In the vicinity of the leading edge, the velocity tends to increase rapidly. Hence, a relatively high-velocity gradient takes place, and the skin friction is at maximum values at all of the investigated
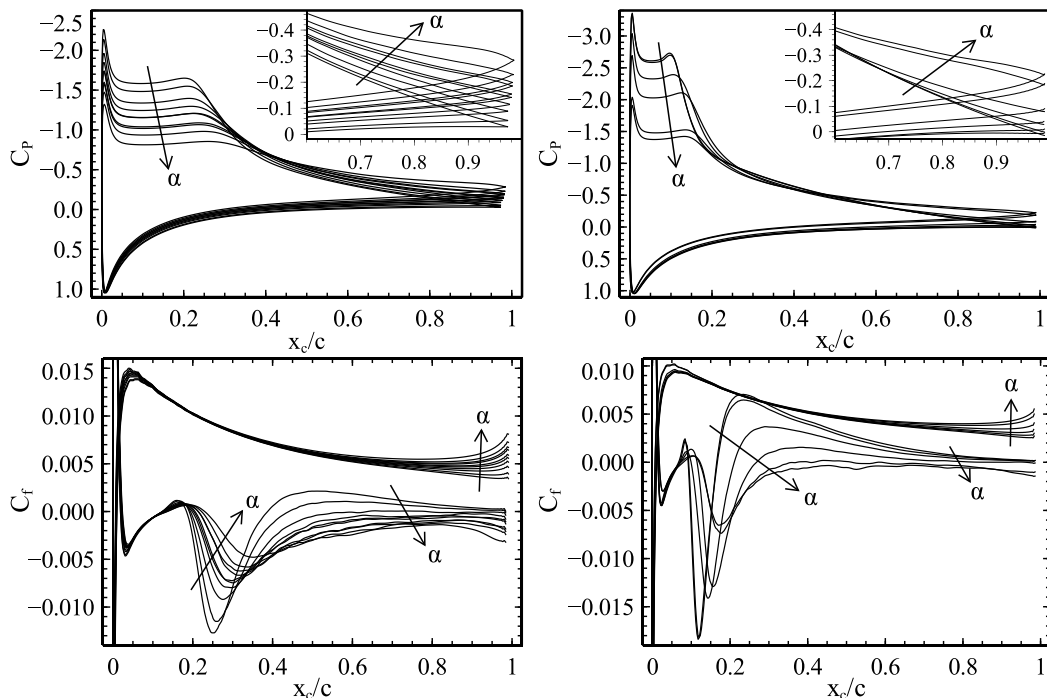
FIG. 5. Locally time-averaged pressure and skin-friction coefficients plotted versus the distance from the airfoil leading edge x_c/c. The arrows indicate the direction in which the angle of attack, α, increases in ascending order.

angles of attack as seen in the figure. Downstream the leading edge, on the suction surface, the flow separates as a consequence of the high-velocity gradient and the APG. Thus, the skin friction drops sharply until it crosses the x-axis and becomes negative. The secondary vortex, illustrated in Fig. 3, rotates in the anticlockwise direction and induces a positive skin friction. Hence, the skin friction becomes positive again. Downstream the secondary vortex, the skin friction is influenced by the recirculating flow inside the LSB which is rotating in the clockwise direction and produces negative skin friction. The skin friction becomes positive downstream the LSB for angles of attack lower than the angle of attack of maximum LFO. At angles of attack higher than the stall angle of attack the flow field separates, again, downstream the LSB and upstream the trailing edge. The flow reattaches to the airfoil surface at the trailing edge and the TEB forms. Consequently, the skin-friction coefficient becomes negative again in the region occupied by the TEB. On the pressure surface, the skin-friction coefficient increases in the vicinity of the trailing edge as the angle of attack increases due to the acceleration of the flow. At angles of attack higher than the angle of attack of maximum LFO, the LSB and TEB merge and form a separated flow region that spans the whole airfoil chord in the mean sense; thus, the skin friction is negative on the entire suction surface of the airfoil.

Eight profiles of the streamwise velocity component were extracted along local vertical axes. The local axes are located at distance x_c/c measured from the airfoil leading edge along the airfoil chord. Figure 6 shows comparison of the extracted data along the local vertical axes with the incompressible experimental data of Ohtake and Motohashi [42] and Ohtake [43]. The experimental data were acquired at $Re_c = 5 \times 10^4$ using hot-wire anemometry. The discrepancy in the velocity
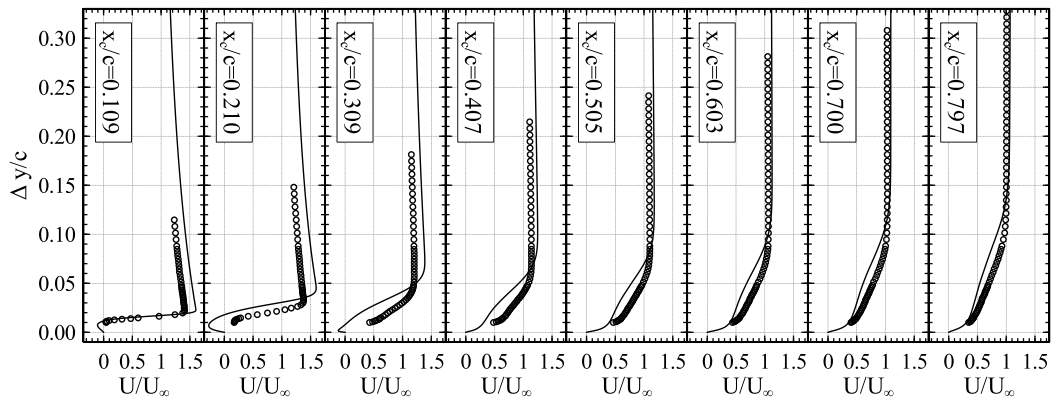
FIG. 6. Profiles of the scaled mean (U/U_∞) of the streamwise velocity plotted versus vertical distance from the airfoil surface ($\Delta y/c$) at eight locations (x_c/c) measured from the leading edge along the airfoil chord at $\mathrm{Re}_c = 5 \times 10^4$ and $\alpha = 9.0°$. Solid line: LES data; circles: incompressible experimental data of Ohtake and Motohashi [42] and Ohtake [43] at $\mathrm{Re}_c = 5 \times 10^4$.

near the wall is due to the fact that the hot wire can measure only positive velocities, and negative velocities are interpreted as positive velocities with the same magnitude. Furthermore, the hot-wire anemometry does not recognize which velocity component cools its wire; thus, it overestimates the streamwise velocity component at locations where the wall-normal velocity component has significant magnitude. Also, the LESs were carried out at a free-stream Mach number of 0.4, whereas the experiment was conducted at incompressible flow conditions. Thus, the discrepancy can also be attributed to the effect of compressibility.

Figure 7 also compares predicted variations of the pressure coefficient and the skin friction around the airfoil surface with the LES data of Alferez *et al.* [19]. As seen in the figure the LES data at $\mathrm{Re}_c = 9 \times 10^4$, $\mathrm{M}_\infty = 0.4$, and the stall angle of attack of $10.25°$ compares very well to the LES data of Alferez *et al.* [19] at $\mathrm{Re}_c = 10^5$, $\mathrm{M}_\infty = 0.16$, and the angle of attack of $10.55°$, which is a little bit lower than the stall angle of attack ($10.55° \leqslant \alpha_s \leqslant 10.8°$). The discrepancy between the LES data of the present work and that of Alferez *et al.* [19] is due to the significant difference in the free-stream Mach number and consequently the effect of compressibility.
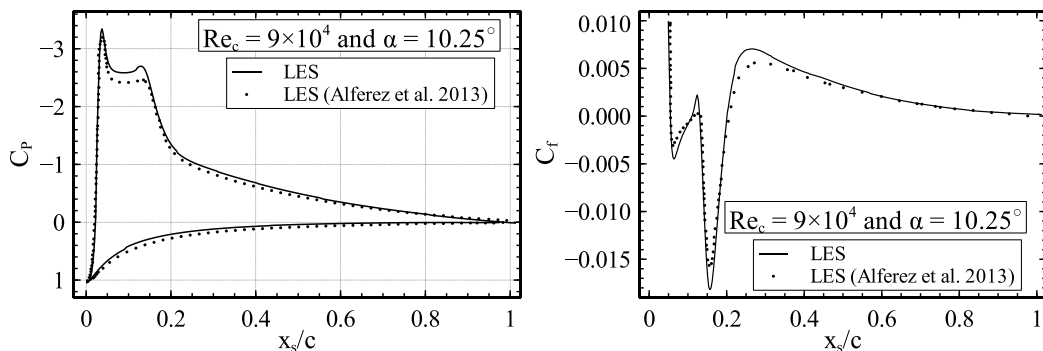

FIG. 7. Profiles of the mean pressure and skin-friction coefficients plotted versus the distance from the airfoil leading edge computed along the curvilinear coordinate on the airfoil suction side x_s/c with $x_s/c = 0$ at the stagnation point at $\mathrm{Re}_c = 9 \times 10^4$ and $\alpha = 10.25°$.
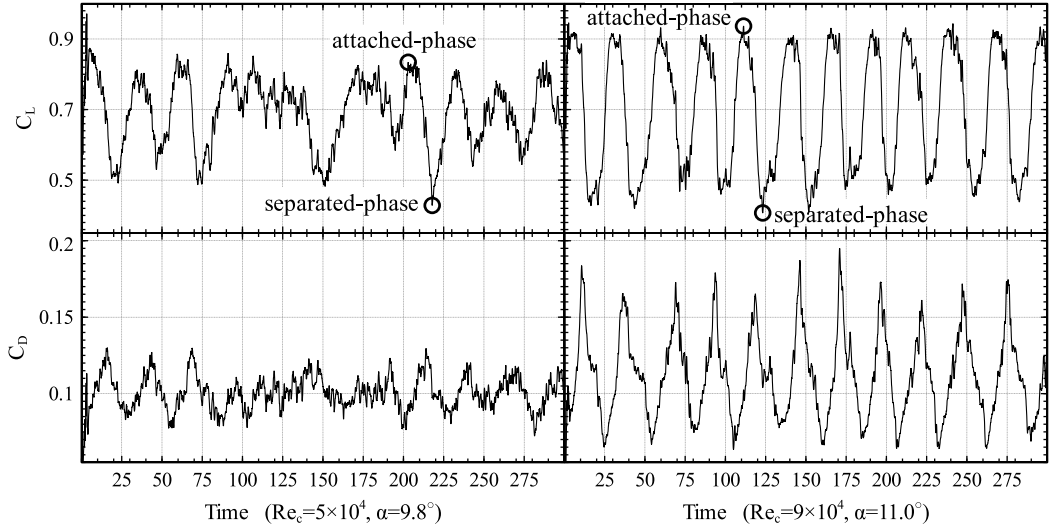
FIG. 8. Time histories of the lift and the drag coefficients.

The pressure coefficient was duly integrated about the airfoil at each time step for each angle of attack to obtain time histories of the lift and the drag coefficients. Time histories of the lift and the drag coefficients are shown in Fig. 8. The black circles shown at the flow time of 202.955 and 217.855 at $Re_c = 5 \times 10^4$, and at the flow time of 111.255 and 123.155 at $Re_c = 9 \times 10^4$ indicate the instants in time when the instantaneous isosurfaces of the λ_2 criterion for the attached and separated phases of the flow field are shown in Fig. 4. The mean lift and drag coefficients at the angles of attack of 9.8° and 11.0° are $(\overline{C_L} = 0.6943, \overline{C_D} = 0.1001)$ and $(\overline{C_L} = 0.7028, \overline{C_D} = 0.1110)$, respectively. Time histories of the lift at the angle of attack of 9.8°, the drag at 9.8°, the lift at 11.0°, and the drag at 11.0° oscillate at an amplitude of about 22%, 25%, 35%, and 50% of their mean values, respectively. At the Reynolds number of 5×10^4 the LFO cycle is disturbed, and only a few cycles resemble each other in a time span of about 10 cycles. As the Reynolds number increases to 9×10^4, the LFO cycle becomes uniform and almost all of the cycles resemble each other.

The drag coefficient consistently peaks when the lift coefficient hits its mean value as seen in the figure. Thus, the lift coefficient is leading the drag coefficient by a phase shift of $\pi/2$. In the present study, only the pressure component of the force is considered. Thus, no phase shift between the lift and the drag is expected. However, these are unsteady aerodynamics studies, and the oscillations in the aerodynamic coefficients arise from the fluctuating pressure. The fluctuating pressure is the sum of several modes, and the most dominant are two low-frequency modes. The first low-frequency mode (LFO mode 1) affects the lift coefficient, and the second low-frequency mode (LFO mode 2) affects the drag coefficient. The LFO mode 1 leads the LFO mode 2 by a phase shift of $\pi/2$, as discussed in Ref. [30]. Thus, the lift leads the drag by a phase shift of $\pi/2$.

Figure 9 illustrates the time-averaged values of the time histories of the lift and the drag coefficients for all of the investigated angles of attack at $Re_c = 5 \times 10^4$ and 9×10^4. The LES data of Almutairi and Alqadi [27] at $Re_c = 5 \times 10^4$ using Grid 1 above presented here to demonstrate how the grid distribution affect the LSB, the LFO, and consequently the variation of the lift coefficient with the angle of attack at near-stall conditions. At Reynolds number of 5×10^4 and 9×10^4 the angles of attack of maximum lift are $\alpha_s = 9.0°$ and 10.25°, respectively. Time-averaged values of the moment and skin-friction coefficients for all of the investigated angles of attack at $Re_c = 5 \times 10^4$ and 9×10^4 are shown in Fig. 10. The experimental data of Ohtake *et al.* [44] was not transformed
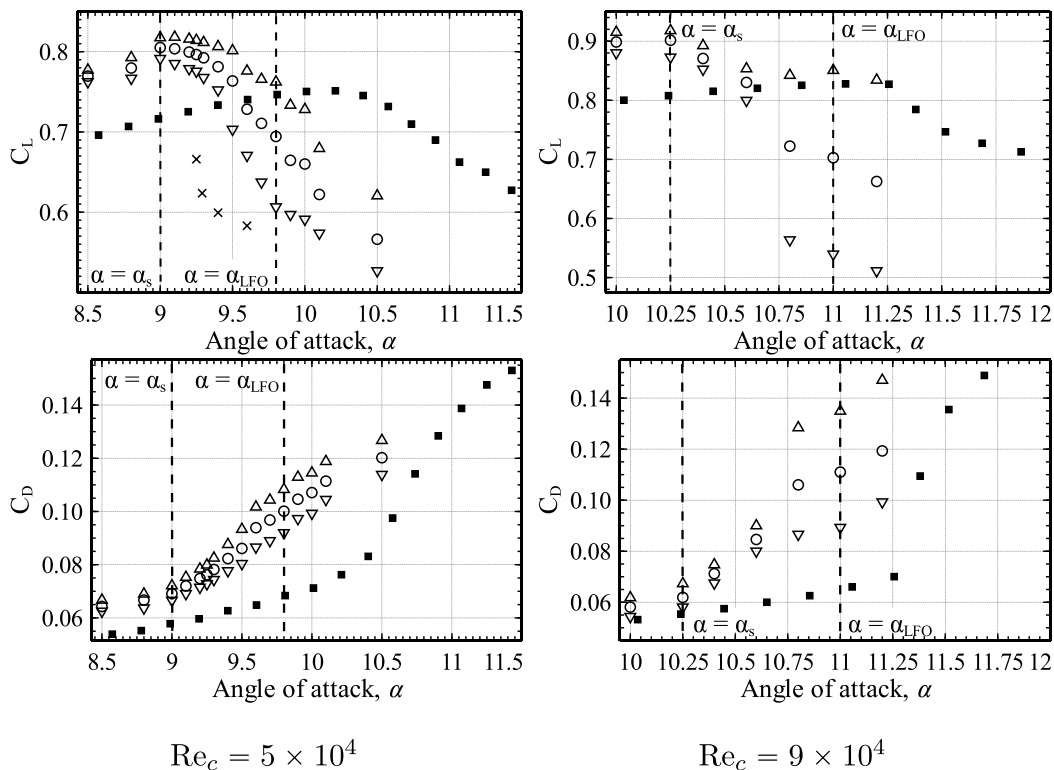
FIG. 9. Mean lift and drag coefficients plotted versus the angle of attack α. Circles, upward triangles, and downward triangles display the mean-lift, high-lift, and low-lift time average of the lift and drag coefficients, respectively. The filled black squares indicate the incompressible data of Ohtake *et al.* [44] at $Re_c = 5 \times 10^4$. The $\times$'s display the LES data of Almutairi and Alqadi [27].

to its compressible counterpart. The effects of compressibility are expressed by the shift in the magnitude of the lift coefficient, and the angle of attack at which the lift has maximum values. Recently, Benton and Visbal [45] showed that increased compressibility causes an earlier inception of dynamic stall as a consequence of bursting of the LSB. Hence, similar effects of compressibility in the case of static stall could affect the transition process of the separated shear layer and the characteristics of the LSB, and consequently lowers the angle of attack of maximum lift.

The aerodynamic coefficients suggest two key angles of attack and three angle-of-attack regimes. The first key angle of attack is the stall angle of attack (α_s), and the second is the angle of attack of maximum LFO (α_{LFO}). The angle-of-attack regimes are (1) $\alpha < \alpha_s$, (2) $\alpha_s \leqslant \alpha < \alpha_{LFO}$, and (3) $\alpha \geqslant \alpha_{LFO}$. As seen in the figures, the aerodynamic coefficients are not much affected by the variations in the LSB in the first angle-of-attack regime. In the second angle-of-attack regime, the aerodynamic coefficients undergo a transition process in which their magnitude is affected by variations in the LSB and the developing LFO. In the third angle-of-attack regime, the effects of the LFO on the aerodynamic coefficients gradually diminishes until the airfoil approaches the angle of a full stall.

The vertical distance between the upward and downward triangle at each angle of attack shows the variation between the high-lift and low-lift time average of the aerodynamic coefficients. The variation between the high-lift and low-lift time average of the aerodynamic coefficients is relatively small, increases in proportion to the angle of attack, and reaches a maximum magnitude in the first, second, and third angle-of-attack regimes, respectively.

$$\mathrm{Re}_c = 5 \times 10^4 \qquad\qquad \mathrm{Re}_c = 9 \times 10^4$$
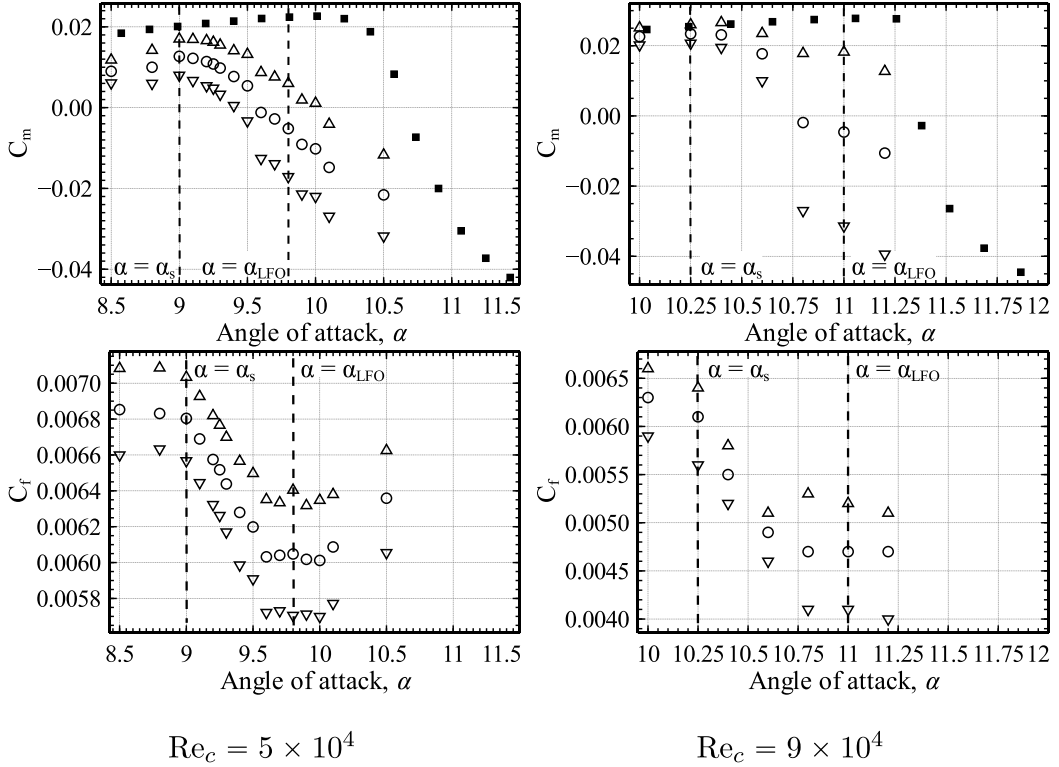
FIG. 10. Mean moment and skin-friction coefficients plotted versus the angle of attack α.

C. Spectral analysis

The magnitude of the time-averaged turbulent kinetic energy (TKE) varies across the separated shear layer. A line which connect the locations of the maximum TKE values is defined as the center of the separated shear layer. Four probes are then located along the center of the separated shear layer. The first probe (Probe 1) is located at the point of separation of the shear layer. Probe 4 is located at a point where the TKE has a maxima. Two other probes (Probe 2 and Probe 3) are located between Probe 1 and Probe 4. The four probes are shown on the time-averaged mean-lift flow fields in Figs. 14, 15, and 16 below for the angles of attack of (9.0°, 10.25°), (9.8°, 11.0°), and (10.5°, 11.2°), respectively. The probes are indicated by the red filled circles and ordered with Probe 1 located at the closest point to the leading edge and Probe 4 located at the furthest downstream point. The center of the separated shear layer is faithfully aligned with the mean dividing streamline as seen in the figures.

The instantaneous values of the streamwise, wall-normal, and spanwise velocities were probed in time at the location of the four probes at each angle of attack. The fast Fourier transform (FFT) algorithm was used to estimate the spectra of the local variables. Figure 11 (top) shows the spectra of local variables recorded at Probes 1–4 at $\mathrm{Re}_c = 5 \times 10^4$ and the angles of attack of 9.0° (stall angle of attack), 9.8° (the angle of attack of maximum LFO), and 10.5° (full stall). The bottom of Fig. 11 shows the spectra of the local variables at $\mathrm{Re}_c = 9 \times 10^4$ and the angles of attack of 10.25°, 11.0°, and 11.2°. The line on the upper right corners of the figures indicates the $-5/3$ slope. The amplitude of the spectra at Probe 1 is shown on the left y-axis, and the amplitude of the spectra for the other probes (Probes 2–4) is shown on the right y-axis.

At Probe 1 the amplitude of the spectra of the local velocities is considerably small compared to its counterpart at the other probes. Also, the amplitude of the spectra of the spanwise velocity
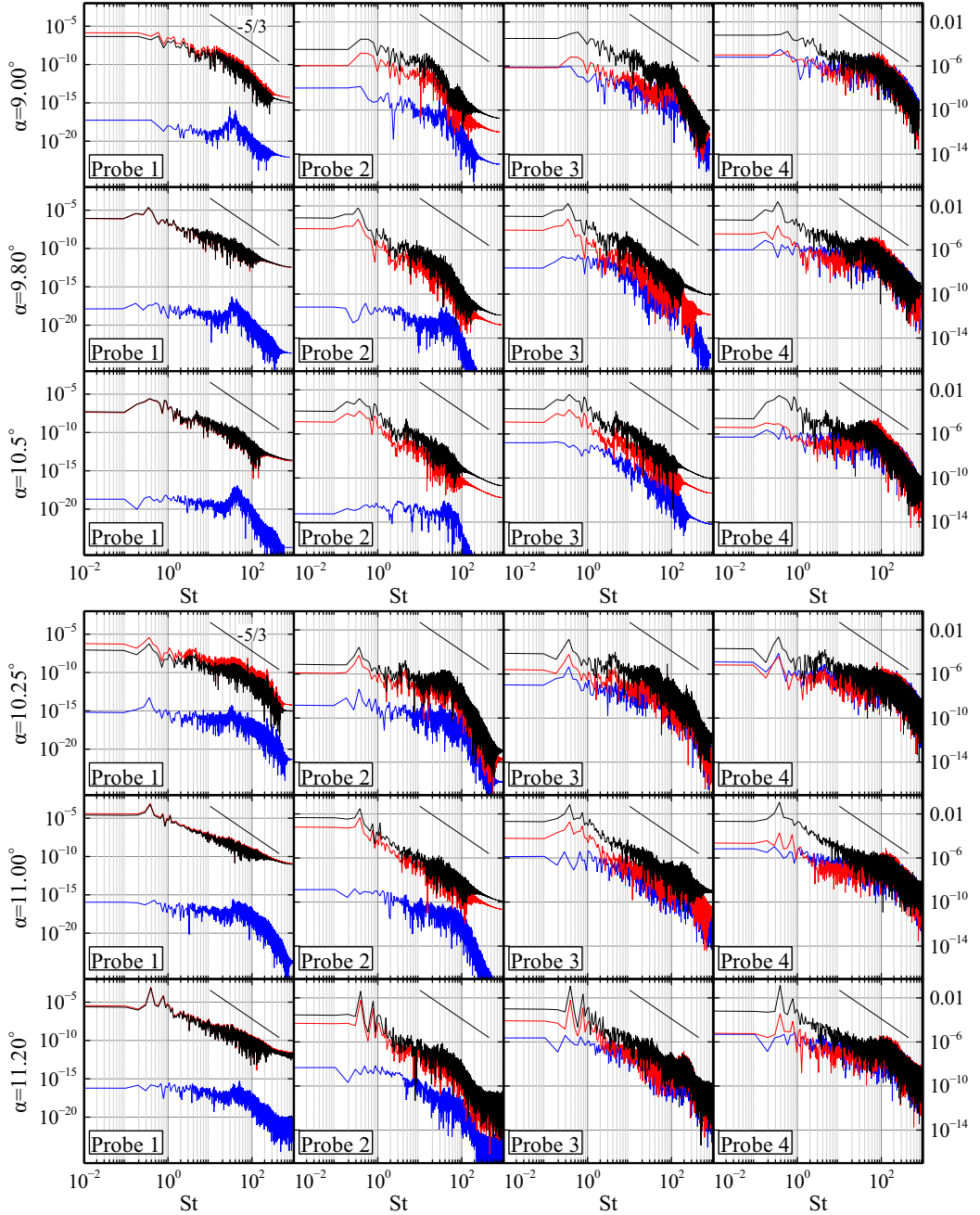
FIG. 11. Spectra of the streamwise (black line), wall-normal (red line), and spanwise (blue line) velocities for the angles of attack of 9.0°, 9.8°, and 10.5° at $\mathrm{Re}_c = 5 \times 10^4$ (top), and the angles of attack of 10.25°, 11.0°, and 11.2° at $\mathrm{Re}_c = 9 \times 10^4$ (bottom).

is very small compared to the spectra of the streamwise and wall-normal velocities at Probe 1. The amplitudes of the spectra of the spanwise velocity increase at Probe 2. The amplitudes of the spectra of the three velocities become comparable to each other at Probe 3, and the streamwise
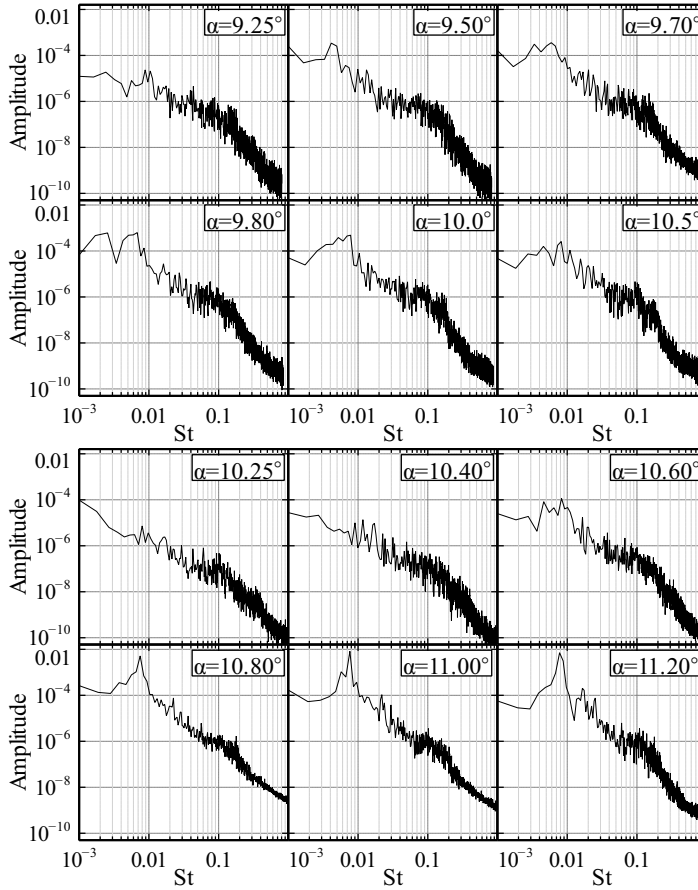
FIG. 12. Spectra of the lift coefficient for the angles of attack $\alpha = 9.25°$–$10.5°$ at $Re_c = 5 \times 10^4$ (top), and $\alpha = 10.25°$–$11.2°$ at $Re_c = 9 \times 10^4$ (bottom).

velocity dominates the other two velocity components. At Probe 4 (the location of the maximum TKE), the spectra have the classical slope of $-5/3$ for the inertial subrange indicating that the flow is turbulent. At the angles of attack of $9.0°$ and $10.25°$ the flow develops more rapidly compared to the flow field at higher angles of attack.

Most of the variations in the pressure field are integrated into the lift coefficient signal. Hence, any globally dominant flow feature is reflected by a peak in the spectrum of C_L. The spectra of the lift coefficient were dully calculated using the FFT algorithm. For each of the 16 angles of attack at $Re_c = 5 \times 10^4$, the spectrum is dominated by a low-frequency peak as seen in Fig. 12. The spectrum of C_L exhibits low-frequency oscillations at the angle of attack of $9.25°$ as a consequence of vortex shedding and shear layer flapping. At angles of attack higher than the stall angle of attack, the flow oscillates at low frequency between attached and separated phases. The LFO continues to develop and gains more strength until the amplitude reaches a maximum at $\alpha_{LFO} = 9.8°$. At angles of attack higher than α_{LFO}, the LFO loses momentum and the amplitude of the C_L spectra diminishes as seen in the figure.

At the Reynolds number of 9×10^4 the spectra do not exhibit low-frequency peaks at angles of attack lower than or equal the stall angle of attack. Thus, vortex shedding and shear layer flapping do not induce low-frequency oscillation at this Reynolds number. At angles of attack higher than the stall angle of attack the flow starts to switch between separated and attached phases as a consequence
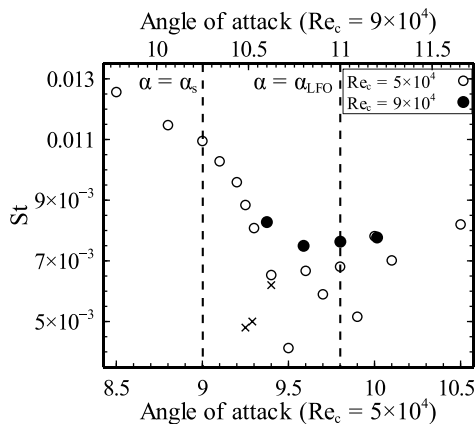
FIG. 13. Low-frequency Strouhal number (St) for the lift coefficient plotted versus the angle of attack α. Circles: LES data, and ×'s: the LES data of Almutairi and Alqadi [27].

of bubble bursting and reformation. Hence, the spectrum at the angle of attack of $9.6°$ exhibits two low-frequency peaks as seen in the figure. The spectra exhibit sharp and pronounced low-frequency peaks at angles of attack $\alpha \geqslant 10.8°$. This is indicative that the LFO at these angles of attack repeats periodically and are more pronounced in the magnitude of oscillation.

Figure 13 shows the Strouhal number of the most dominant low-frequency oscillations, St, plotted versus the angle of attack for the lift coefficient. The ×'s denote the LES data of Almutairi and Alqadi [27] at the angles of attack of $9.25°$, $9.29°$, and $9.4°$. The authors used a coarser grid and consequently overestimated the size of the bubble. Thus, the airfoil in their study undergoes an early full stall at the angle of attack of $9.6°$.

Time histories of the lift coefficient show no apparent low-frequency oscillations for angles of attack lower than the stall angle of attack [28,29]. However, the spectral analysis identified low-frequency modes at these angles of attack at $Re_c = 5 \times 10^4$. The LFO at prestall, where the LSB remains intact, features bubble shedding and breathing modes, whereas the LFO at angles of attack higher than the stall angle of attack features bubble bursting and reformation.

D. The shape and size of the separation bubbles

Figures 14, 15, and 16 show streamlines patterns superimposed on color maps of the conditionally time-averaged streamwise velocity component at the stall angle of attack (α_s), the angle of attack of maximum LFO (α_{LFO}), and an angle of attack higher than α_{LFO}, respectively. The flow field is ensemble averaged in the spanwise direction and conditionally time averaged on three levels of high-lift ($< \widehat{u_i} >$), mean-lift ($< \overline{u_i} >$), and low-lift ($< \bar{u_i} >$) average. As seen in the figures, the LSB is formed on the upper surface of the airfoil. It is noted that the flow is fully attached in the high-lift, mean-lift, and low-lift time average at the stall angle of attack, and the LFO does not have enough momentum to separate the flow. The flow is massively separated (open bubble) in the high-lift, mean-lift, and low-lift time average at the angles of attack of $10.5°$ at $Re_c = 5 \times 10^4$ and $11.2°$ at $Re_c = 9 \times 10^4$; and the LFO does not have enough momentum to reattach the flow. This is indicative that these angles set the limits of the angles of attack of interest. At the angle of attack of maximum LFO, the flow field is fully attached in the high-lift time average and massively separated in the low-lift time average. Hence, the LFO has the maximum magnitude of oscillation to switch the flow from fully attached to massively separated. It is interesting to note that the secondary bubble forms at the same location, in the mean sense, when the flow is attached and when it is massively separated. Furthermore, the current observation being statistical implies that the conditions for the formation of the secondary bubble are permanent in space and stationary in time.
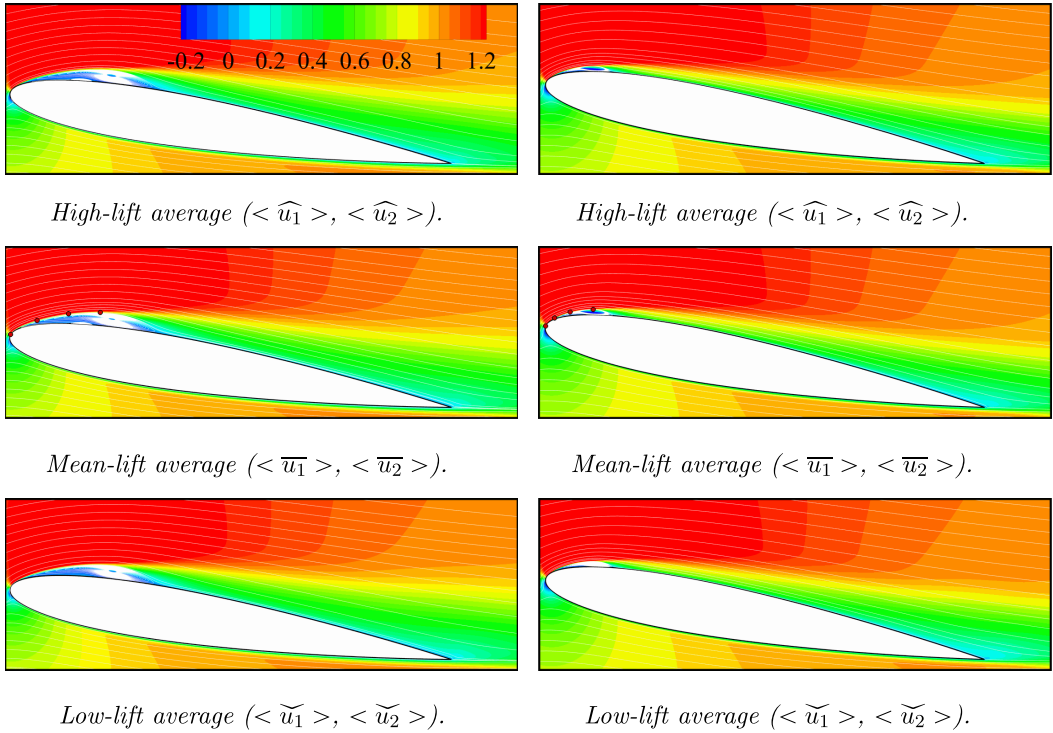
High-lift average ($< \widehat{u_1} >, < \widehat{u_2} >$).

High-lift average ($< \widehat{u_1} >, < \widehat{u_2} >$).

Mean-lift average ($< \overline{u_1} >, < \overline{u_2} >$).

Mean-lift average ($< \overline{u_1} >, < \overline{u_2} >$).

Low-lift average ($< \widetilde{u_1} >, < \widetilde{u_2} >$).

Low-lift average ($< \widetilde{u_1} >, < \widetilde{u_2} >$).

FIG. 14. Streamlines patterns of the time-averaged flow field superimposed on color maps of the time-averaged streamwise velocity component at the stall angle of attack [$\alpha_s = 9.0°$ at $\mathrm{Re}_c = 5 \times 10^4$ (left), and $\alpha_s = 10.25°$ at $\mathrm{Re}_c = 9 \times 10^4$ (right)].

A trailing-edge separation region that constitutes the TEB forms at the stall angle of attack ($\alpha_s = 9.0°$ at $\mathrm{Re}_c = 5 \times 10^4$ and $\alpha_s = 10.25°$ at $\mathrm{Re}_c = 9 \times 10^4$). The TEB grows in size as the angle of attack increases. The LSB and the TEB merge, in the mean sense, at the angle of attack of maximum oscillations in the LFO ($\alpha_{LFO} = 9.8°$ at $\mathrm{Re}_c = 5 \times 10^4$ and $\alpha_{LFO} = 11.0°$ at $\mathrm{Re}_c = 9 \times 10^4$). The merged bubbles continue to deform, and an open bubble forms when the airfoil approaches the angle of a full stall ($\alpha = 10.5°$ at $\mathrm{Re}_c = 5 \times 10^4$ and $\alpha > 11.2°$ at $\mathrm{Re}_c = 9 \times 10^4$). Thus, a TEB forms at the stall angle of attack and merges with the LSB at the angle of maximum LFO, and the merged bubbles forms an open bubble as the airfoil approaches the angle of attack of a full stall. This type of stall is a combination of thin-airfoil and trailing-edge stall as classified by Mccullough and Gault [31].

Broeren and Bragg [23] studied the flow field around an LRN(1)–1007 airfoil at $\mathrm{Re}_c = 3 \times 10^5$ and the angle of attack of $\alpha = 15°$. Two velocity components were measured at 687 locations in the x-y plane at the airfoil midspan using laser Doppler velocimeter (LDV). A conditional-averaging method was used and 24 time slots within one cycle resolved the oscillation in 15° intervals. They showed four snapshots of contours of the streamwise velocity at four different phases. The snapshots show small leading-edge and trailing-edge separated zones; they grow in the second snapshot, merge in the third one, and become an open bubble in the fourth snapshot. Their experimental observations are in good agreement with the present discussion inequities of how limited and coarse their data are.

Figures 17 and 18 illustrate the mean length and the mean height of the LSB and the TEB plotted versus the angle of attack. The mean length and the mean height of the bubbles were obtained by approximating the separation location (point **S** in Fig. 3) and the reattachment location (point **R**
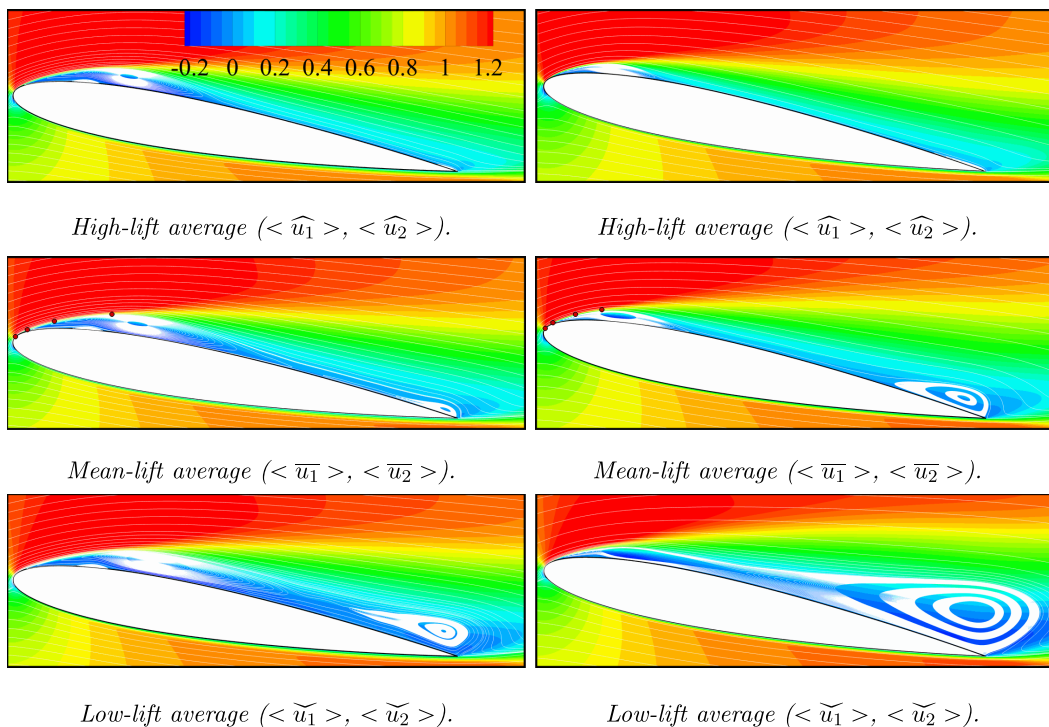
High-lift average ($< \widehat{u_1} >, < \widehat{u_2} >$).

High-lift average ($< \widehat{u_1} >, < \widehat{u_2} >$).

Mean-lift average ($< \overline{u_1} >, < \overline{u_2} >$).

Mean-lift average ($< \overline{u_1} >, < \overline{u_2} >$).

Low-lift average ($< \breve{u_1} >, < \breve{u_2} >$).

Low-lift average ($< \breve{u_1} >, < \breve{u_2} >$).

FIG. 15. Streamlines patterns of the time-averaged flow field superimposed on color maps of the time-averaged streamwise velocity component at the angle of attack of maximum LFO [$\alpha_{LFO} = 9.8°$ at $Re_c = 5 \times 10^4$ (left), and $\alpha_{LFO} = 11.0°$ at $Re_c = 9 \times 10^4$ (right)].

in Fig. 3). At angles of attack lower than the angle of attack of maximum LFO ($\alpha < \alpha_{LFO}$), the LSB is bounded by two half-saddle at points **S** and **R** as shown in Fig. 3. The TEB is also bounded by two half-saddle points at the separation point upstream the trailing edge and the reattachment point at the trailing edge. The length of the LSB and the TEB, in the mean sense, is measured from the separation point to the reattachment point. The TEB forms at angles of attack equal or higher than the stall angle of attack ($\alpha \geqslant \alpha_s$). Thus, the length and height of the TEB are not defined for angles of attack lower than the stall angle of attack. At angles of attack equal or higher than the angle of attack of maximum LFO ($\alpha \geqslant \alpha_{LFO}$), the LSB and the TEB merge and form a full saddle at the merging point. Therefore, the length and the height of the LSB and the TEB are not defined for angles of attack equal or higher than the angle of attack of maximum LFO. The height of the bubbles was measured across each bubble from the airfoil surface, passing through the bubble focus, and to the edge of the bubble.

The LSBs have a minimum length at the stall angle of attack at each Reynolds number. The height of the LSBs is proportional to the angle of attack. The LSBs are shorter and thinner at the Reynolds number of 9×10^4 than their corresponding ones at $Re_c = 5 \times 10^4$. The length of the TEBs is very small at the inception of stall and increases gradually with the angle of attack. As the LFOs gain considerable magnitude of oscillations, the length of the TEBs abruptly increases as seen in the figure. Figure 19 shows the ratio of the height of the LSBs to their length plotted versus the angle of attack. At angles of attack higher than the stall angle of attack, the bubble bursts. Thus, the LSBs become thinner, in the mean sense, as the angle of attack increases.

At angles of attack lower than the stall angle of attack, the LSB remains intact. As the angle of attack increases, the bubble bursts to form a long bubble. Diwan *et al.* [13] refined the bursting criterion developed by Gaster [7] to take into consideration the effect of the height of the LSB
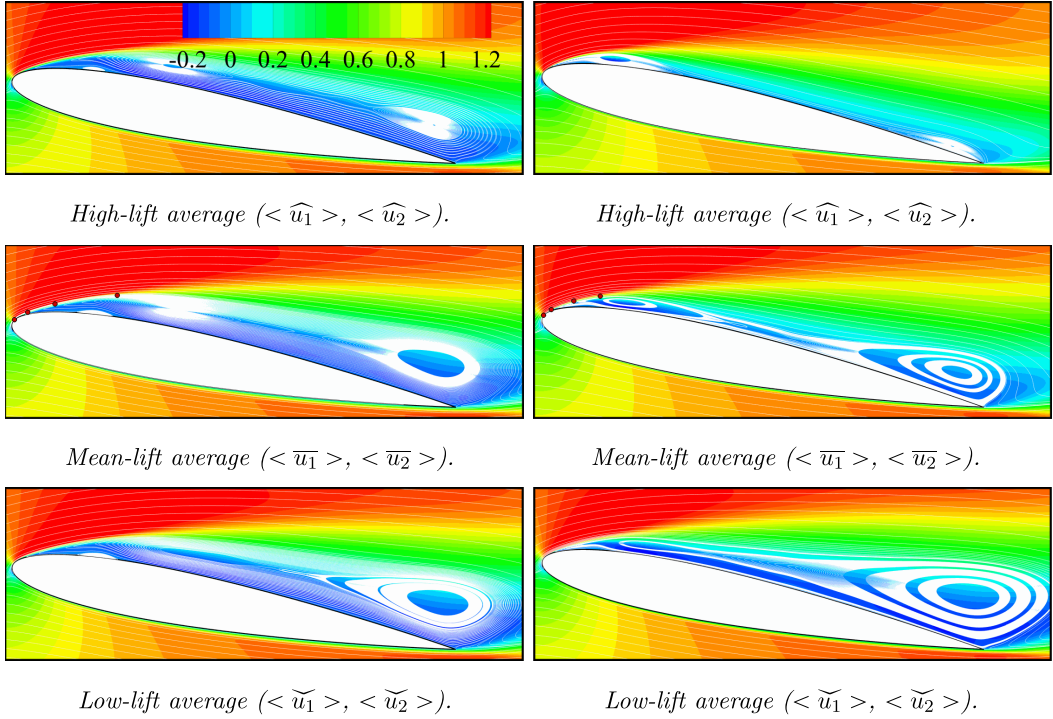
High-lift average (< $\widehat{u_1}$ >, < $\widehat{u_2}$ >).

High-lift average (< $\widehat{u_1}$ >, < $\widehat{u_2}$ >).

Mean-lift average (< $\overline{u_1}$ >, < $\overline{u_2}$ >).

Mean-lift average (< $\overline{u_1}$ >, < $\overline{u_2}$ >).

Low-lift average (< $\widetilde{u_1}$ >, < $\widetilde{u_2}$ >).

Low-lift average (< $\widetilde{u_1}$ >, < $\widetilde{u_2}$ >).

FIG. 16. Streamline patterns of the time-averaged flow field superimposed on color maps of the time-averaged streamwise velocity component for $\alpha = 10.5°$ at $\mathrm{Re}_c = 5 \times 10^4$ (left), and $\alpha = 11.2°$ at $\mathrm{Re}_c = 9 \times 10^4$ (right).

in addition to its length. The bursting parameter is given by $P_h = \frac{h^2}{\nu} \frac{\Delta U}{\Delta x}$, where h is the height of the LSB, ν is the kinematic viscosity, ΔU is the velocity difference across the bubble, and Δx is the length of the LSB. The Reynolds number based on the height of the bubble is given by
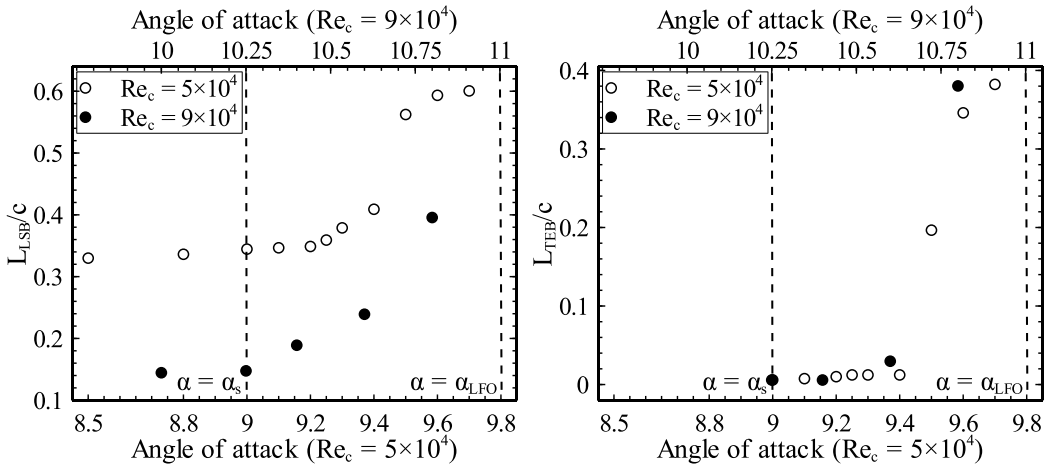
FIG. 17. The length of the Laminar Separation Bubble (LSB) and the Trailing-Edge Bubble (TEB) plotted versus the angle of attack α.
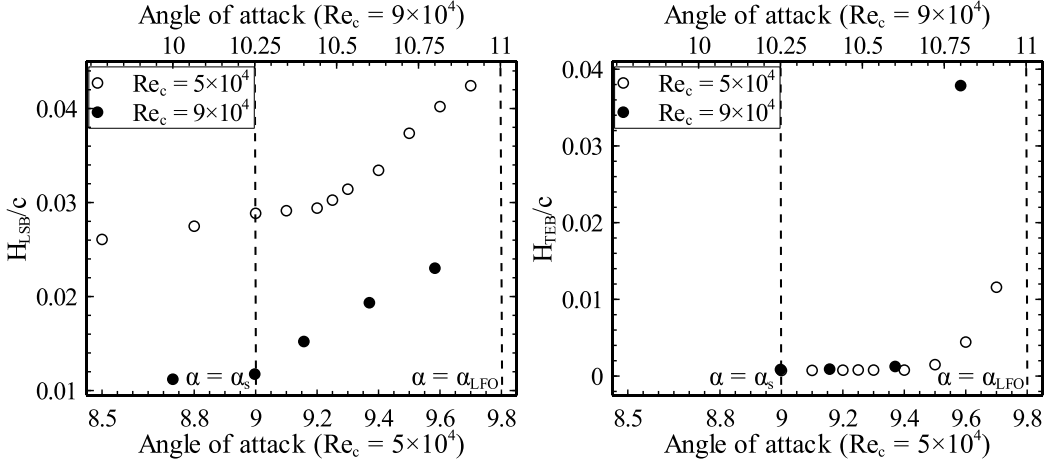
FIG. 18. The height of the Laminar Separation Bubble (LSB) and the Trailing-Edge Bubble (TEB) plotted versus the angle of attack α.

$\mathrm{Re}_h = \frac{U_h h}{\nu}$, where U_h is the velocity at the maximum height of the LSB (h). The bubble is termed short if $P_h > -28$. The right-hand side of Fig. 19 shows a plot of the bursting parameter P_h versus the Reynolds number Re_h. As seen in the figure, the bursting criterion suggests that the LSBs at Reynolds number of 5×10^4 and angles of attack lower than the stall angle of attack are short bubbles—in total agreement with the definition of s short bubble and the above discussion which shows that the LSBs are long bubbles at angles of attack higher than the stall angle of attack. The bursting parameter P_h is proportional to h^2, and the LSBs are thinner at $\mathrm{Re}_c = 9 \times 10^4$ than their $\mathrm{Re}_c = 5 \times 10^4$ counterparts. Thus, the criterion suggests that all of the LSBs at the Reynolds number of 9×10^4 are short bubbles as seen in the figure.

Figure 20 shows the variation of the maximum reverse velocity (MRV) inside the bubble as a percentage of the free-stream velocity, denoted by circles and as a percentage of the maximum
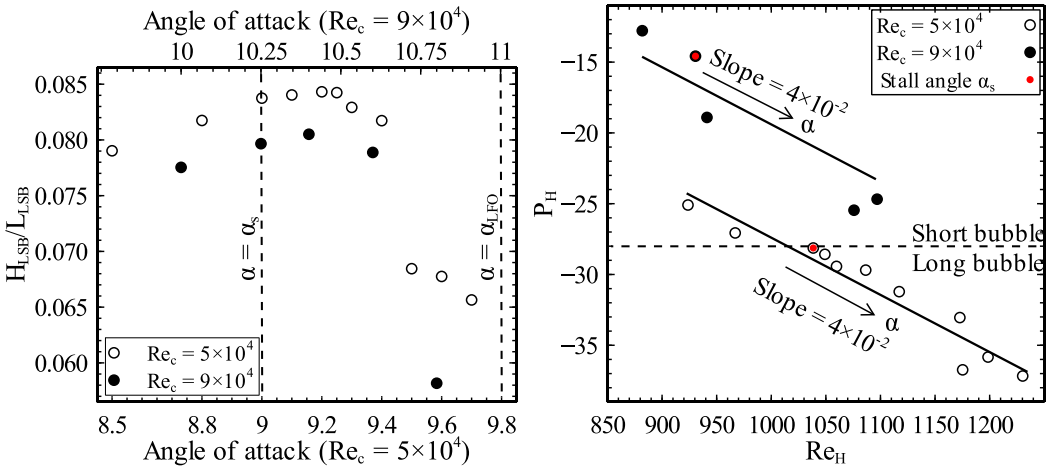
FIG. 19. The aspect ratio of the LSB plotted versus the angle of attack α (left). The bursting parameter P_h plotted versus the Reynolds number Re_h. The arrows indicate the direction in which the angle of attack, α, increases in ascending order (right).

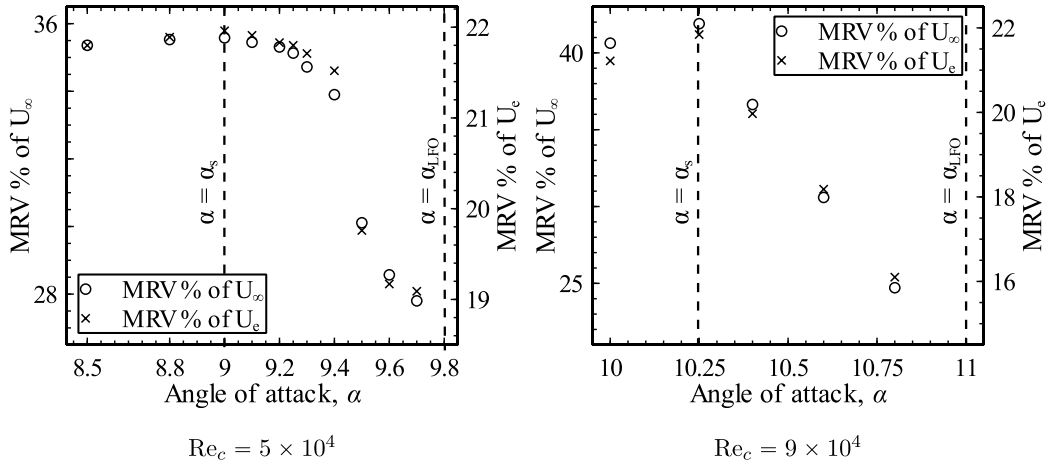$$\text{Re}_c = 5 \times 10^4 \qquad\qquad \text{Re}_c = 9 \times 10^4$$

FIG. 20. Maximum reverse velocity (MRV) plotted versus the angle of attack α.

external velocity outside the bubble, denoted by $\times$'s. The MRV reaches a maximum of 22% of the maximum external velocity outside the bubble and a maximum of about 35.6% of the free-stream velocity at the angle of attack of $9.0°$ at $\text{Re}_c = 5 \times 10^4$. At the Reynolds number of 9×10^4, the MRV reaches a maximum of 21.8% of the maximum external velocity outside the bubble and a maximum of 41.9% of the free-stream velocity at the angle of attack of $10.25°$. It is worth mentioning that at angles of attack higher than the stall angle of attack, the flow field is switching between an attached phase and a separated phase. Thus, the percentage of the MRV is in fact the average of the percentage when the flow is attached and when it is separated. The study by Alam and Sandham [9] showed that the separation bubble is considered absolutely unstable if the separation bubble sustains a maximum reverse velocity percentage in the range MRV = 15% to 20%. The MRV for the current simulation, 22%, is larger than the range pointed out by Alam and Sandham [9] and can be considered as an indication of the presence of an absolute instability in the bubble at the stall angle of attack.

E. Periodic and turbulent fluctuations of the flow field

Figures 21, 22, and 23 illustrate color maps of the variance of the velocity components $(\overline{\breve{u}_i^2})$ at the stall angles of attack, at the angles of attack of maximum LFO (α_{LFO}), and at angles of attack higher than α_{LFO}, respectively. Where $\breve{u}_i$ is the summation of the periodic and the turbulent fluctuations as defined in Eq. (5) or the total fluctuations. As seen in the figures, $\overline{\breve{u}_i^2}$ have considerable magnitude along the separated shear layer in the vicinity of the leading edge where the Kelvin-Helmholtz instability extracts kinetic energy from the mean flow and feeds it into the turbulent fluctuations. $\overline{\breve{u}_i^2}$ also have significant magnitude along the shear layer in the vicinity of the trailing edge where kinetic energy is fed into the turbulent fluctuations. On the suction surface of the airfoil, $\overline{\breve{u}_i^2}$ have considerable magnitude where a triad of three vortices extracts kinetic energy from the mean flow and adds it to the periodic fluctuations as proposed by Eljack and Soria [30].

Figures 24, 25, and 26 show the maximum values of the velocity variance arising from the periodic fluctuations $(\overline{u_i''^2})$, the velocity variance arising from the turbulent fluctuations $(\overline{u_i'^2})$, and the turbulent kinetic energy (TKE) plotted versus the angle of attack, where u_i'' is the periodic fluctuations and u_i' is the turbulent fluctuations. The triad of vortices generates, controls, and sustains the LFO [30]. Also, the triad of vortices adds periodic fluctuations to the flow field; thus, statistics of the periodic fluctuations have their maximum magnitude at the angle of attack of maximum oscillations in the LFO (α_{LFO}). The maximum values of the turbulent statistics peak at α_s. The flow

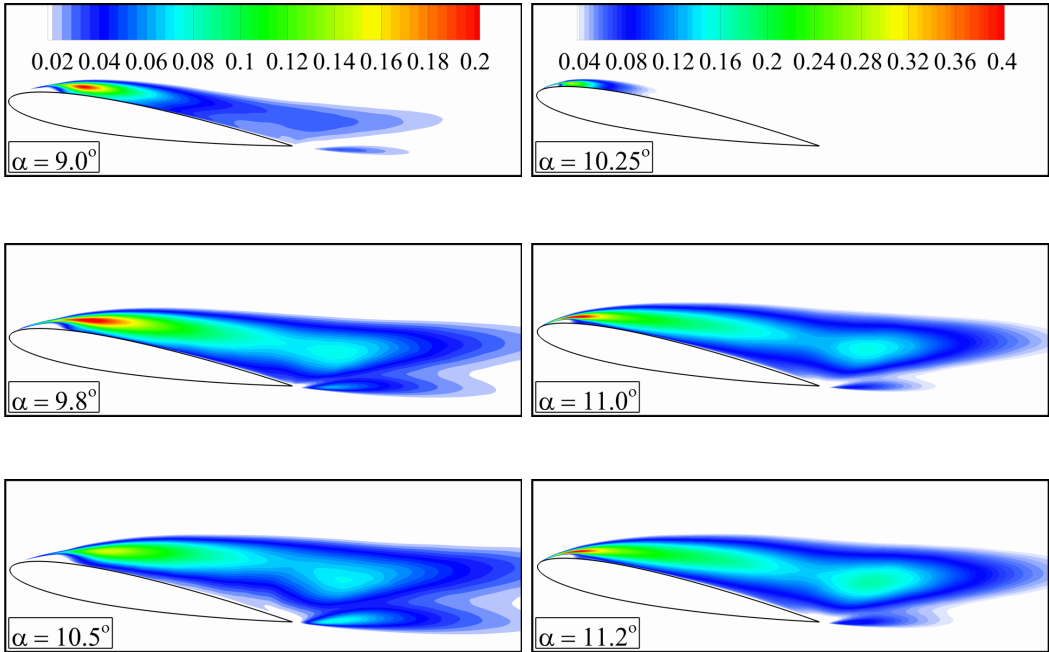FIG. 21. Color map of the variance of the streamwise velocity component arising from the total fluctuations $(\overline{\breve{u}_1^2})$ at $\mathrm{Re}_c = 5 \times 10^4$ (left) and $\mathrm{Re}_c = 9 \times 10^4$ (right).
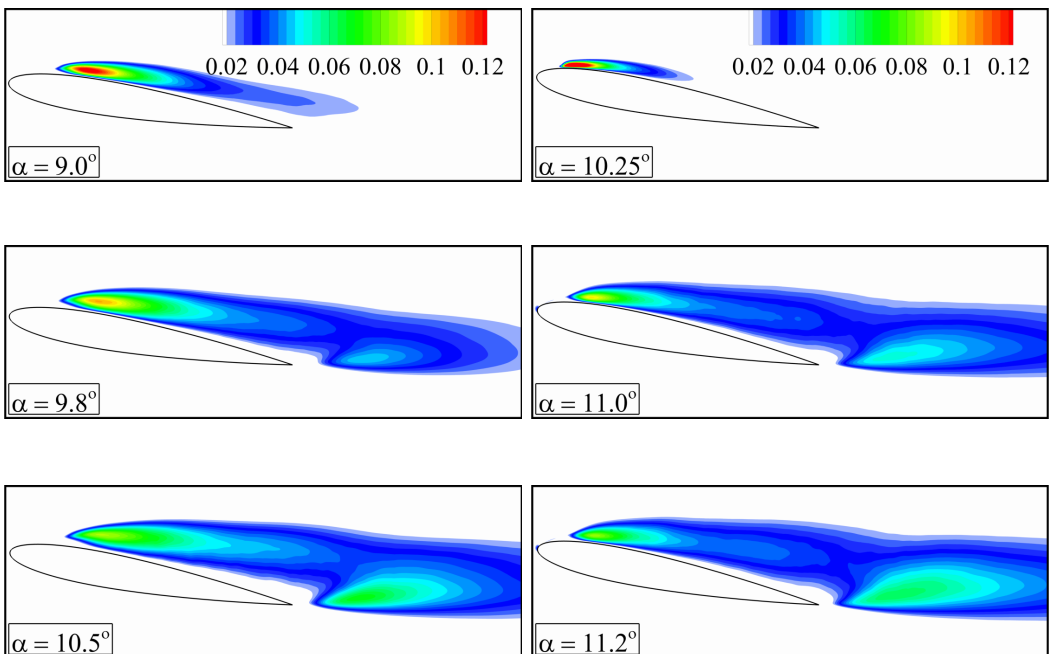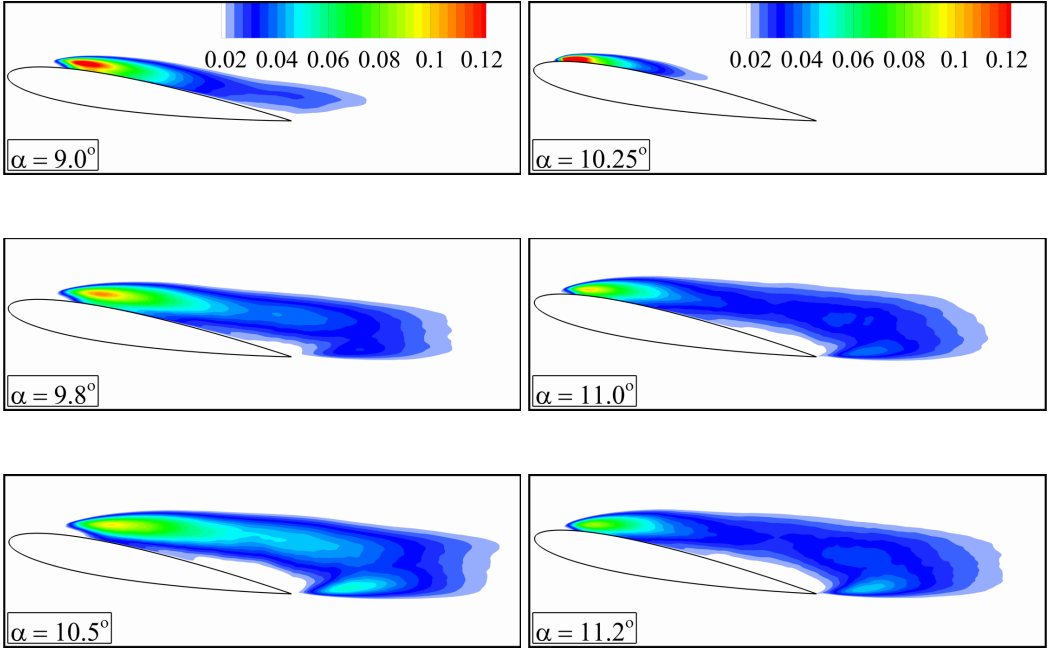

FIG. 22. Color map of the variance of the wall-normal velocity component arising from the total fluctuations $(\overline{\breve{u}_2^2})$ at $\mathrm{Re}_c = 5 \times 10^4$ (left) and $\mathrm{Re}_c = 9 \times 10^4$ (right).

FIG. 23. Color map of the variance of the spanwise velocity component arising from the total fluctuations ($\overline{\breve{u}_3^2}$) at $\mathrm{Re}_c = 5 \times 10^4$ (left) and $\mathrm{Re}_c = 9 \times 10^4$ (right).

field is periodic in the spanwise direction, and the mean velocity component in this direction is zero. Hence, the periodic oscillations in the spanwise direction (u_3'') is not shown because it is not defined. The only acting velocity in this direction is the spanwise turbulent fluctuations (u_3'), and it is responsible for the break-down of the two-dimensional rolls into three-dimensional structures.

Figure 27 shows color maps of turbulence production ($-\breve{u}_1\breve{u}_2 \frac{\partial \overline{u}_1}{\partial y}$), arising from the total fluctuations, at selected key angles of attack. Turbulence production is dependent on Reynolds stress and
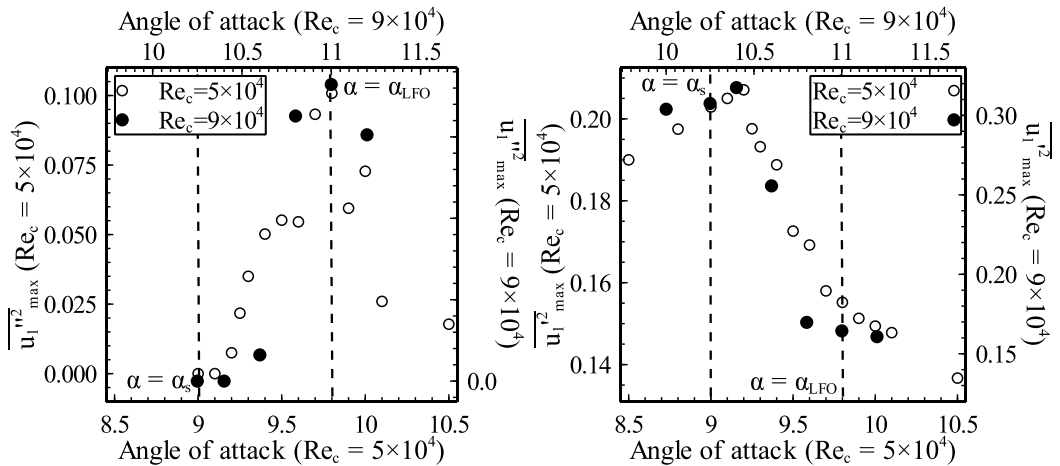
FIG. 24. Maximum values of the variance of the streamwise velocity component arising from the periodic fluctuations ($\overline{u_1''^2}$) (left) and from the turbulent fluctuations ($\overline{u_1'^2}$) (right) plotted versus the angle of attack α.
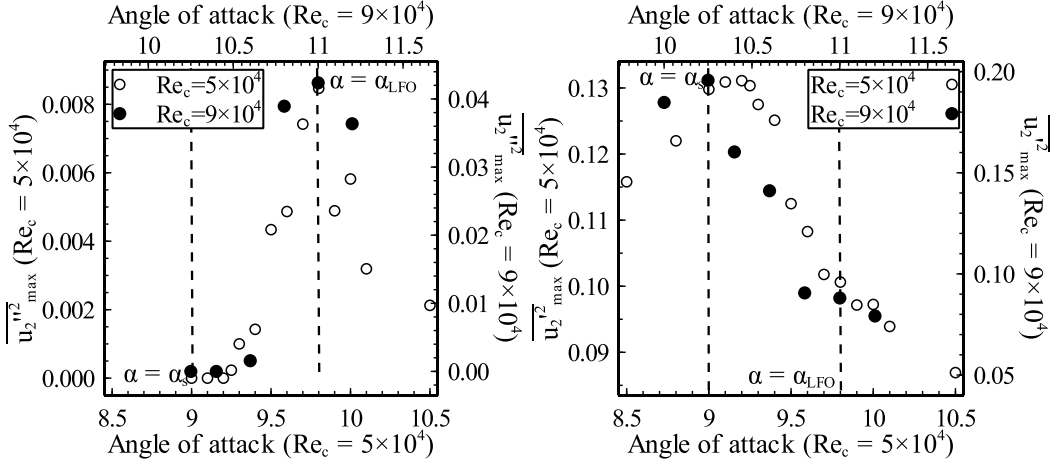
FIG. 25. Maximum values of the variance of the wall-normal velocity component arising from the periodic fluctuations ($\overline{u_2''^2}$) (left) and from the turbulent fluctuations ($\overline{u_2'^2}$) (right) plotted versus the angle of attack α.

the gradient of the mean velocity. Reynolds stress extracts energy from the mean flow and feeds it into the fluctuations along the separated shear layer via the Kelvin-Helmholtz instability. The mean velocity above the LSB increases during the attached phase and decreases during the separated phase as seen in Figs. 14, 15, and 16. Consequently, the gradient of the mean velocity increases during the attached phase and decreases during the separated phase. Thus, production of turbulence is affected by the Kelvin-Helmholtz instability along the separated shear layer and changes in the gradient of the mean velocity due to the dynamics of the triad of vortices on the suction surface of the airfoil [30].

Figure 28 illustrates maximum values of the turbulence production ($-\overline{\breve{u}_1 \breve{u}_2} \frac{\partial \overline{u_1}}{\partial y}$) and its distance from the airfoil leading edge ($\Delta x/c$) plotted versus the angle of attack α. The maximum values of the turbulence production arising from the total fluctuations have their maxima at the stall angle of
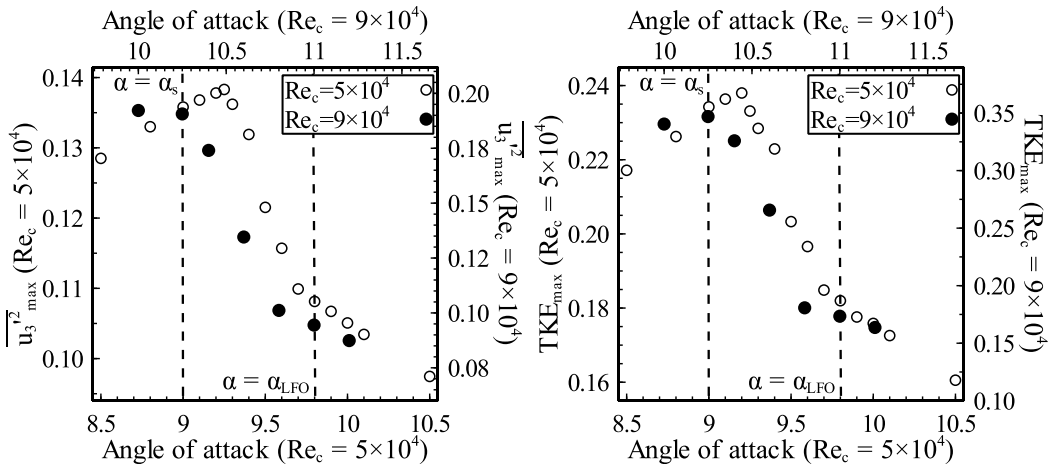

FIG. 26. Maximum values of the variance of the spanwise velocity component arising from the turbulent fluctuations ($\overline{u_3'^2}$) (left) and maximum Turbulent Kinetic Energy (TKE) (right) plotted versus the angle of attack α.
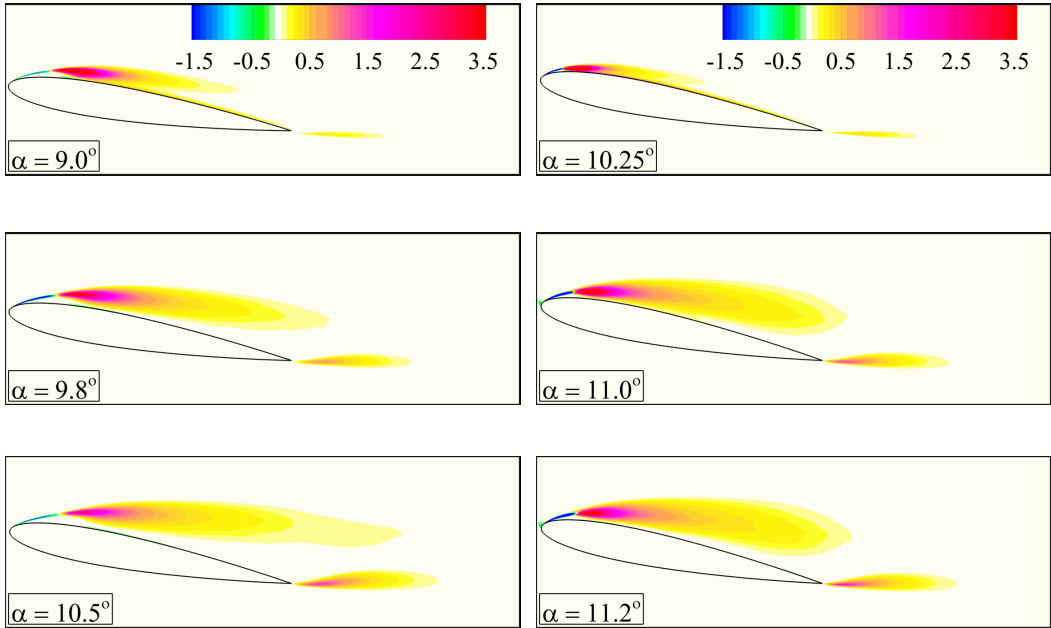
FIG. 27. Color map of the turbulence production arising from the total fluctuations ($-\bar{\breve{u}}_1\breve{u}_2 \frac{\partial \overline{u_1}}{\partial y}$) at $\mathrm{Re}_c = 5 \times 10^4$ (left) and $\mathrm{Re}_c = 9 \times 10^4$ (right).

attack. The location of the maximum turbulence production moves towards the airfoil leading edge and becomes closest to it at the stall angle of attack, and moves away from the leading edge as the angle of attack increases above the stall angle of attack. The location of the maximum turbulence production moves away from the airfoil surface as the angle of attack increases in total agreement with Almutairi and Alqadi [27]. Color maps and the maximum values of the variance of the pressure ($\overline{\breve{p}^2}$) are shown in Figs. 29 and 30. The variance of pressure fluctuations has significant magnitude in
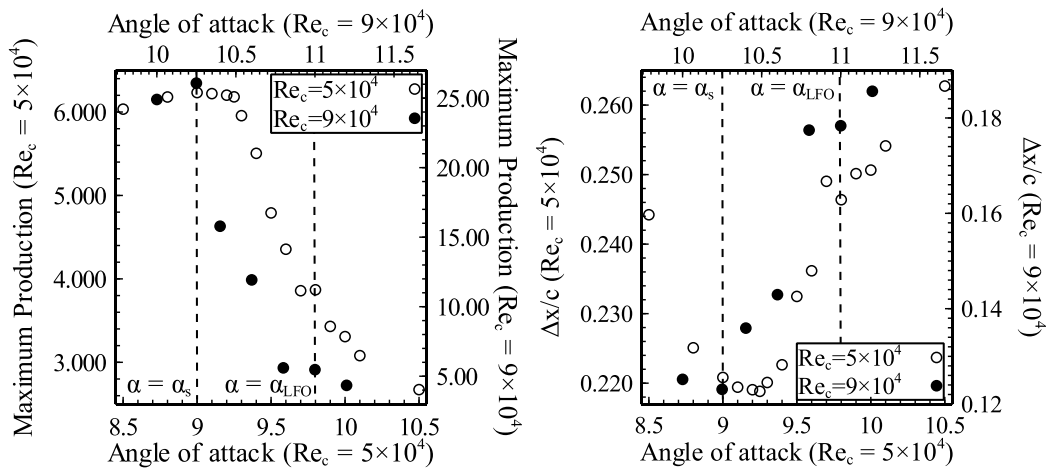

FIG. 28. Maximum values of the turbulence production arising from the total fluctuations ($-\bar{\breve{u}}_1\breve{u}_2 \frac{\partial \overline{u_1}}{\partial y}$) (left) and the distance of the maximum turbulence production measured from the airfoil leading edge ($\Delta x/c$) (right) plotted versus the angle of attack α.
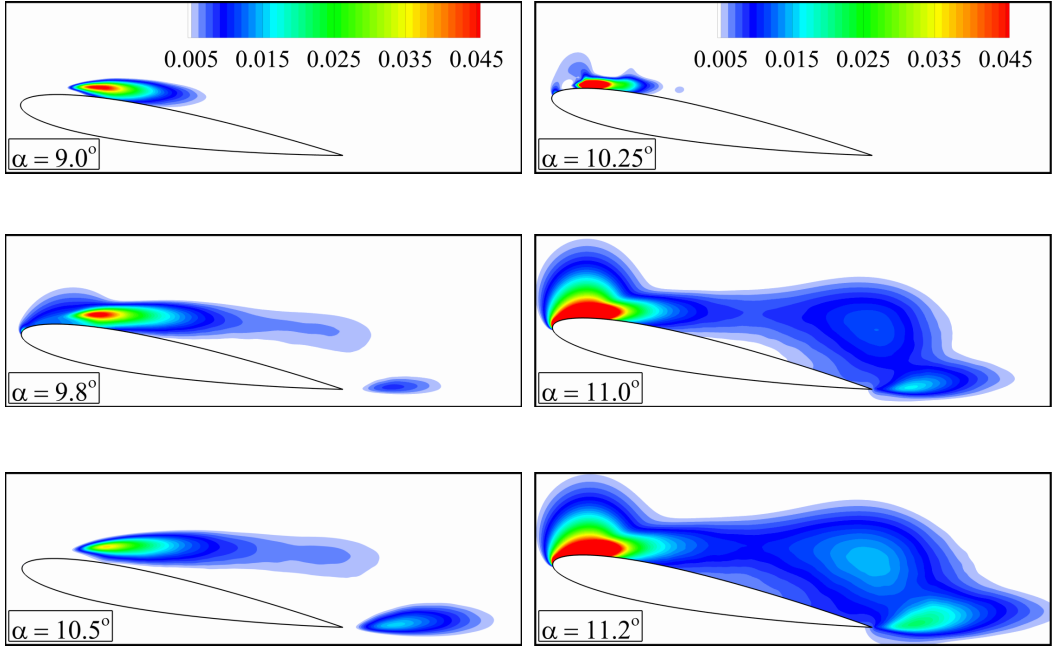
FIG. 29. Color map of the variance of the pressure arising from the total fluctuations ($\overline{\tilde{p}^2}$) at $Re_c = 5 \times 10^4$ (left) and $Re_c = 9 \times 10^4$ (right).

the laminar portion of the separated shear layer. This is indicative that the instability that generates and sustains the LFO originates at this location. It is worth mentioning that each of these figures has four axis two for the magnitude of the maximum variance, and two for the sets of angles of attack at each Reynolds number.
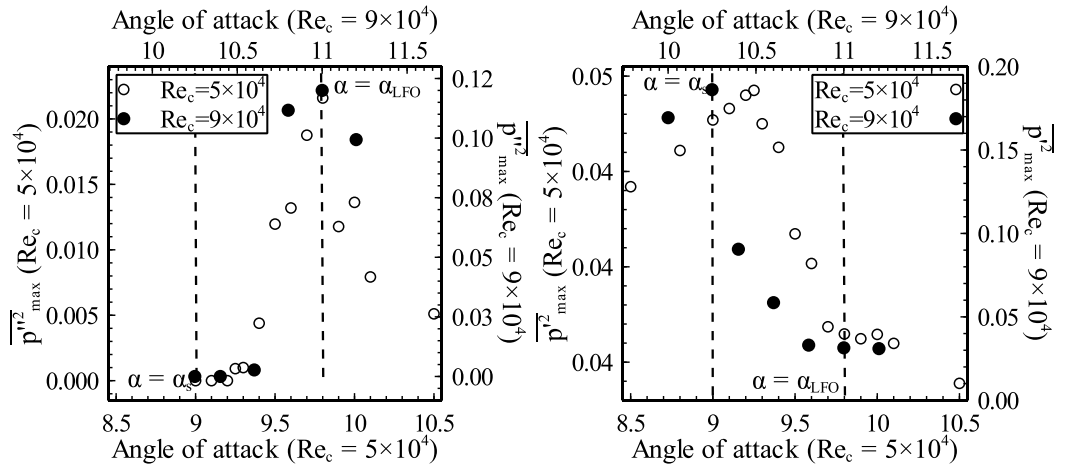

FIG. 30. Maximum values of the variance of the pressure arising from the periodic fluctuations ($\overline{p'^2}$) (left) and from the turbulent fluctuations ($\overline{p'^2}$) (right) plotted versus the angle of attack α.

VI. CONCLUSIONS

Large eddy simulations were carried out for the flow field about a NACA-0012 airfoil at Reynolds number of 5×10^4 and 9×10^4, Mach number of 0.4, and several angles of attack near stall. The objective of the study was to examine the effects of the angle of attack on the characteristics of the flow field, the laminar separation bubble (LSB), and its associated low-frequency flow oscillation (LFO). Statistics of the flow field show that there are two key angles of attack: The stall angle of attack and the angle of attack of maximum LFO. Statistics of the periodic flow peak at the angle of attack of maximum LFO, and statistics of the fluctuating flow (turbulent fluctuations) peak at the stall angle of attack. At angles of attack lower than the stall angle of attack the mean flow field is attached, a short bubble forms, and the LFO does not have sufficient momentum to separate the flow field. At angles of attack higher than the stall angle of attack and lower than the angle of attack of maximum LFO, the flow field undergoes a transition process in which the LFO develops until the flow field reaches a quasiperiodic switching between separated and attached flow, and the LSB switches between short and long bubble. At angles of attack higher than the angle of attack of maximum LFO, the mean flow field is massively separated, an open bubble forms, and the strength of the LFO gradually decays and becomes unable to reattach the flow until the airfoil approaches the angle of a full stall.

[1] I. Tani, Low-speed flows involving bubble separations, Prog. Aerosp. Sci. **5**, 70 (1964).

[2] T. Mueller, E. Reshotko, N. A. T. O. A. G. for Aerospace Research, and D. F. D. Panel, *Low Reynolds Number Vehicles* (North Atlantic Treaty Organization, Advisory Group for Aerospace Research and Development, 1985).

[3] P. R. Owen and L. Klanfer, *On the laminar boundary layer separation from the leading edge of a thin aerofoil*, RAE Rep. Aero. 2508, October (1953); reissued as A.R.C. CP 220 (1955).

[4] B. Melvill Jones, Stalling, J. R. Aeronaut. Soc. **38**, 753 (1934).

[5] A. D. Young and H. P. Horton, Some results of investigation of separation bubbles, in *AGARD Conference Proceedings CP No. 4* (AGARD, 1966), pp. 780–811.

[6] H. P. Horton, Laminar separation bubbles in two and three dimensional incompressible flow, Ph.D. thesis, University of London, 1968.

[7] M. Gaster, *The structure and behavior of laminar separation bubbles*, Aeronautical Research Council, Reports and Memoranda, No. 3595 (Her Majesty's Stationery Office, London, 1967).

[8] U. Maucher, U. Rist, M. Kloker, and S. Wagner, Dns of laminar-turbulent transition in separation bubbles, in *High Performance Computing in Science and Engineering 99* (Springer, 2000), pp. 279–294.

[9] M. Alam and N. D. Sandham, Direct numerical simulation of 'short' laminar separation bubbles with turbulent reattachment, J. Fluid Mech. **410**, 1 (2000).

[10] C. P. Häggmark, C. Hildings, and D. S. Henningson, A numerical and experimental study of a transitional separation bubble, Aerosp. Sci. Technol. **5**, 317 (2001).

[11] U. Rist and U. Maucher, Investigations of time-growing instabilities in laminar separation bubbles, Eur. J. Mech. B **21**, 495 (2002).

[12] O. Marxen, M. Lang, U. Rist, and S. Wagner, A combined experimental/numerical study of unsteady phenomena in a laminar separation bubble, Flow Turb. Combust. **71**, 133 (2003).

[13] S. S. Diwan, S. J. Chetan, and O. N. Ramesh, On the bursting criterion for laminar separation bubbles, in *IUTAM Symposium on Laminar-Turbulent Transition* (Springer Netherlands, 2006), pp. 401–407.

[14] O. Marxen, D. You, and P. Moin, Numerical simulations of the bursting of a laminar separation bubble and its relation to airfoil stall, in *Advances in Turbulence XI, Springer Proceedings Physics*, Vol. 117, edited by J. Palma and A. S. Lopes (Springer, Berlin, 2007), pp. 712–714.

[15] S. S. Diwan and O. N. Ramesh, On the origin of the inflectional instability of a laminar separation bubble, J. Fluid Mech. **629**, 263 (2009).

[16] O. Marxen and U. Rist, Mean flow deformation in a laminar separation bubble: Separation and stability characteristics, J. Fluid Mech. **660**, 37 (2010).

[17] O. Marxen and D. S. Henningson, The effect of small-amplitude convective disturbances on the size and bursting of a laminar separation bubble, J. Fluid Mech. **671**, 1 (2011).

[18] O. Marxen, M. Lang, and U. Rist, Vortex formation and vortex breakup in a laminar separation bubble, J. Fluid Mech. **728**, 58 (2013).

[19] N. Alferez, I. Mary, and E. Lamballais, Study of stall development around an airfoil by means of high fidelity large eddy simulation, Flow Turbul. Combust. **91**, 623 (2013).

[20] K. B. M. Q. Zaman, D. J. McKinzie, and C. L. Rumsey, A natural low-frequency oscillation of the flow over an airfoil near stalling conditions, J. Fluid Mech. **202**, 403 (1989).

[21] M. B. Bragg, D. C. Heinrich, F. A. Balow, and K. B. M. Q. Zaman, Flow oscillation over an airfoil near stall, AIAA J. **34**, 199 (1996).

[22] A. Broeren and M. Bragg, Low-frequency flowfield unsteadiness during airfoil stall and the influence of stall type, in *AIAA Paper 98-2517* (American Institute of Aeronautics and Astronautics, 1998), pp. 196–209.

[23] A. P. Broeren and M. B. Bragg, Flowfield measurements over an airfoil during natural low-frequency oscillations near stall, AIAA J. **37**, 130 (1999).

[24] A. P. Broeren and M. B. Bragg, Spanwise variation in the unsteady stalling flowfields of two-dimensional airfoil models, AIAA J. **39**, 1641 (2001).

[25] H. Tanaka, Flow visualization and PIV measurements of laminar separation bubble oscillating at low frequency on an airfoil near stall, in *International Congress of the Aeronautical Sciences, Yokohama, Japan* (International Council of the Aeronautical Sciences, Bonn, Germany, 2004), pp. 1–15.

[26] K. Rinoie and N. Takemura, Oscillating behaviour of laminar separation bubble formed on an aerofoil near stall, Aeronaut. J. **108**, 153 (2004).

[27] J. Almutairi and I. Alqadi, Large-eddy simulation of natural low-frequency oscillations of separating-reattaching flow near stall conditions, AIAA J. **51**, 981 (2013).

[28] E. Eljack, High-fidelity numerical simulation of the flow field around a NACA-0012 aerofoil from the laminar separation bubble to a full stall, Int. J. Comput. Fluid Dyn. **31**, 230 (2017).

[29] Y. A. Elawad and E. M. Eljack, Numerical investigation of the low-frequency flow oscillation over a NACA-0012 aerofoil at the inception of stall, Int. J. Micro Air Vehicles **11**, 1 (2019).

[30] E. M. Eljack and J. Soria, Investigation of the low-frequency oscillations in the flowfield about an airfoil, AIAA J. **58**, 4271 (2020).

[31] G. B. Mccullough and D. E. Gault, Examples of three representative types of airfoil-section stall at low speed, Tech. Rep. 2502, National Advisory Committee for Aeronautics (1951).

[32] M. Inagaki, T. Kondoh, and Y. Nagano, A mixed-time-scale SGS model with fixed model-parameters for practical LES, J. Fluids Eng. **127**, 1 (2005).

[33] A. Yoshizawa, K. Kobayashi, T. Kobayashi, and N. Taniguchi, A nonequilibrium fixed-parameter subgrid-scale model obeying the near-wall asymptotic constraint, Phys. Fluids **12**, 2338 (2000).

[34] M. R. Visbal and D. P. Rizzetta, Large-eddy simulation on curvilinear grids using compact differencing and filtering schemes, J. Fluids Eng. **124**, 836 (2002).

[35] J. Almutari, Large-eddy simulation of flow around an airfoil at low Reynolds number near stall, Ph.D. thesis, University of Southampton, 2011.

[36] L. E. Jones, R. D. Sandberg, and N. D. Sandham, Stability and receptivity characteristics of a laminar separation bubble on an aerofoil, J. Fluid Mech. **648**, 257 (2010).

[37] M. H. Carpenter, J. Nordström, and D. Gottlieb, A stable and conservative interface treatment of arbitrary spatial accuracy, J. Comput. Phys. **148**, 341 (1999).

[38] H. S. Sandhu and N. D. Sandham, Boundary conditions for spatially growing compressible shear layers, Tech. Rep., QMW-EP-1100, Queen Mary and Westfield College, University of London (1994).

[39] R. D. Sandberg and N. D. Sandham, Nonreflecting zonal characteristic boundary condition for direct numerical simulation of aerodynamic sound, AIAA J. **44**, 402 (2006).

[40] N. D. Sandham, Q. Li, and H. C. Yee, Entropy splitting for high-order numerical simulation of compressible turbulence, J. Comput. Phys. **178**, 307 (2002).

[41] L. E. Jones, Numerical studies of the flow around an airfoil at low Reynolds number, Ph.D. thesis, University of Southampton, 2008.

[42] T. Ohtake and T. Motohashi, Flow field around NACA0012 airfoil at low Reynolds numbers: Part 1 characteristics of airfoil wake, J. Jpn. Soc. Aeronaut. Space Sci. **57**, 397 (2009).

[43] T. Ohtake, Flow field around NACA0012 airfoil in low Reynolds numbers: Part 2 characteristics of boundary layer, J. Jpn. Soc. Aeronaut. Space Sci. **64**, 123 (2016).

[44] T. Ohtake, Y. Nakae, and T. Motohashi, Nonlinearity of the aerodynamic characteristics of NACA0012 aerofoil at low Reynolds numbers, J. Jpn. Soc. Aeronaut. Space Sci. **55**, 439 (2007).

[45] S. I. Benton and M. R. Visbal, Effects of compressibility on dynamic-stall onset using large-eddy simulation, AIAA J. **58**, 1194 (2020).